THE UNIVERSITY OF MICHIGAN

INDUSTRY PROGRAM OF THE COLLEGE OF ENGINEERING

ELASTIC SCATTERING OF 1.1 BEV POSITIVE PIONS BY PROTONS
AND THE ELASTIC SCATTERING OF 582 MEV PROTONS BY PROTONS

Leonard O. Roellig

A dissertation submitted in partial fulfillment
of the requirements for the degree of
Doctor of Philosophy in the
University of Michigan
1959

January, 1959

IP-349

Doctoral Committee:

<div style="margin-left:2em">

Professor Donald A. Glaser, Chairman
Professor Kenneth M. Case
Associate Professor Paul V. C. Hough
Associate Professor W. Wayne Meinke
Professor Marcellus L. Wiedenbeck

</div>

ACKNOWLEDGMENTS

TABLE OF CONTENTS

LIST OF TABLES

LIST OF FIGURES

I. INTRODUCTION

1. High Energy Pion-Nucleon and Nucleon-Nucleon Scattering

Measurements of pion-nucleon and nucleon-nucleon scattering cross sections have been of great importance to the understanding of meson physics and in the investigation of nuclear forces. Although no single model has been successful in describing all experimental scattering results, the energy dependence of the scattering cross sections has provided powerful clues for determining the form an all inclusive model must assume for various energies.

To illustrate this, consider Figure 1, which shows the total cross section for pion-proton scattering as a function of energy. At low energies only a few angular momentum states are important, and the experimental data can be adequately described by means of a phase shift analysis. The pronounced maximum in the positive pion cross section at 195 Mev reaches a value of 200 mb, which for $j = 3/2$ is very closely equal to $2\pi \mkern-4mu\raise2pt\hbox{$\scriptstyle 2$}\mkern-6mu\lambda^2 (2j+1)$, the maximum value of the cross section for an elastic process occurring in a state with total angular momentum $j=3/2$. ($\lambda = 2\pi\mkern-6mu\lambda$ is the de Broglie wave length in the center of mass system.) Moreover, at this energy the ratio of the total π^+-p cross section to the total π^--p cross section is quite close to 3, which is the ratio of the weight of the isotopic spin state 3/2 in the π^+-p system to that of the state 3/2 in the π^--p system. Thus, a second inference naturally follows: the strong interaction, which peaks at 195 Mev, is characteristic of a state with total isotopic spin $T = 3/2$. A second resonance for the total π^--p cross section is observed at 900 Mev. Since the total
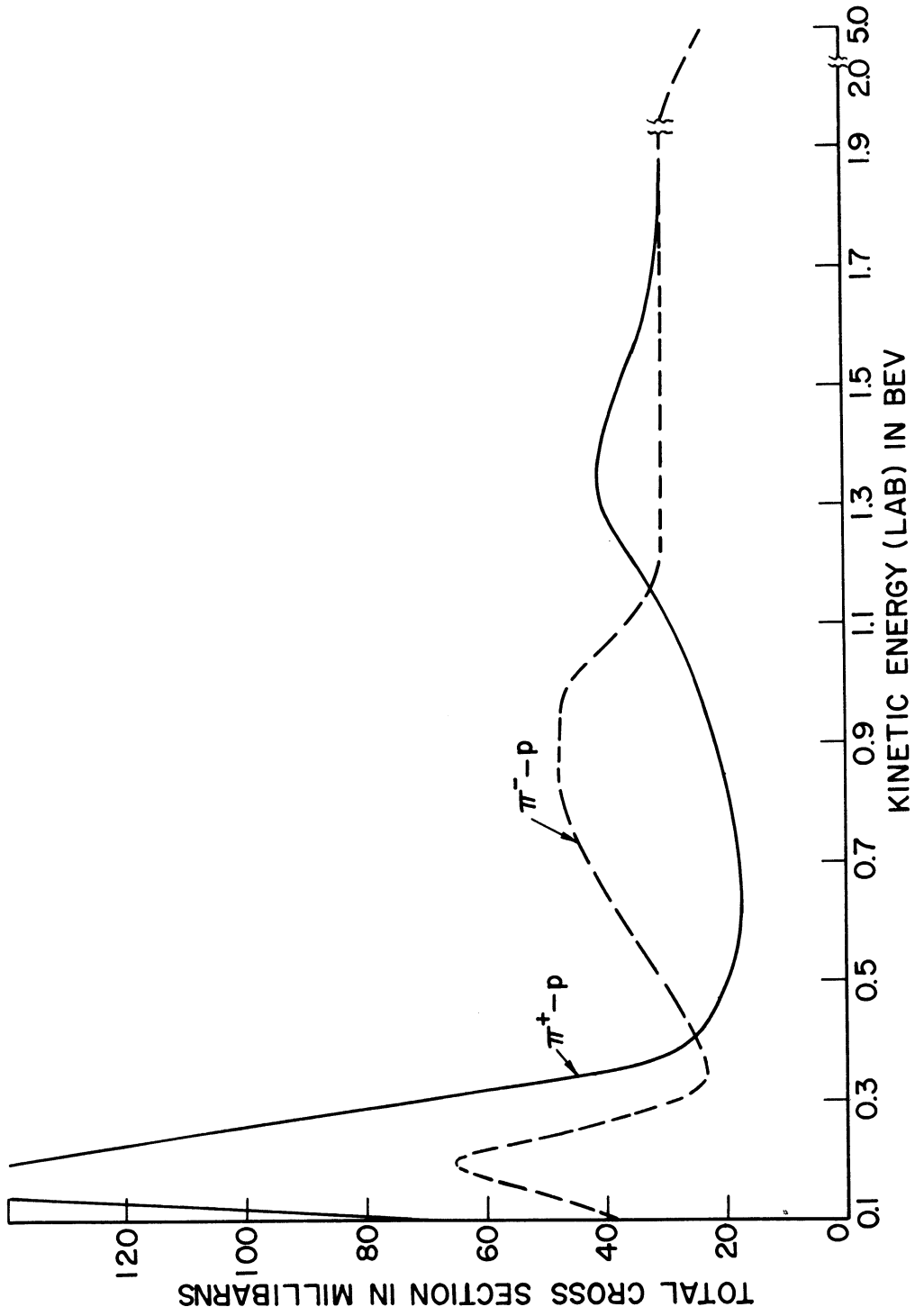
Figure 1. Total Cross Section for π^+-p and π^--p Scattering (For experimental points see References 3-12, 28.)

π^+-p cross section does not show a maximum at this energy, it is natural to assume that the excess scattering must occur in states of total isotopic spin T = 1/2. Yang has calculated that the maximum contribution to the total cross section from a state with T = 1/2 and total angular momentum j is limited by $\sigma \leq \frac{4\pi}{3} \lambdabar^2 \left(2j+1\right) \sigma_e/\sigma_t$, where σ_e is the elastic cross section, and σ_t is the total cross section.[22] Letting σ_e/σ_t = 1/3, this would imply j $\geq$ 11/2, which is highly unlikely at this energy. Dyson[1] and Takeda[2] have proposed to explain the π^--p scattering data at 900 Mev by considering that the interaction between a pion and a proton occurs mainly via an interaction of the bombarding pion, π_b, with a virtual pion, π_v, in the charge cloud around the proton. If the resonant state has T = 0, it will contribute nothing to π^+-p scattering at this energy. The excess scattering will be observed in several angular momentum states of the π^--p system simultaneously. The maximum excess cross section as given by Dyson is $\sigma = \frac{4\pi}{3} \lambdabar^2 (2I+1) F$, where I is the angular momentum of the resonant state, $\lambdabar$ = 7.87 x 10^{-14} cm is now the de Broglie wave length divided by 2π in the center of mass system of the two pions, and F is the probability of finding a positive pion in the proton charge cloud. Because the pion is a boson (T = 0 states must have even parity), only even values of I are allowed, and it is found that the observed scattering can be accounted for with I as low as 0 or 2. Some authors[3], however, have argued that the momentum distribution of virtual pions (they have assumed the momentum of the virtual pion would be of the order μc where μc^2 is the rest energy of the pion) would make any such resonance much broader than the observed peak. Very recently, however, it has been proposed that the π -p

resonant final state may be very important, and this may tend to select the momentum of the virtual pion so that the effective momentum spread is really less.[4]

At high energies (an energy of the incident pion of the order of or greater than 1 Bev) a great many angular momentum states (there are waves of at least ℓ = 0,1,2,3 units of angular momentum participating) must be considered to describe the scattering process, and it is not possible to fit unambiguously the experimental data by means of a phase shift analysis. If one examines the high energy π^--p scattering data in detail[5-12,28], it will be found that the elastic scattering exhibits a large differential cross section for small scattering angles and a rather isotropic differential cross section for large scattering angles. Also the inelastic scattering is much greater, about a factor of 3, than the elastic scattering. It is thus possible to consider the nucleon as an absorbing body which can cause diffraction scattering. Indeed the curve for the π^--p forward elastic scattering does resemble a diffraction curve. The role of diffraction scattering is clear if one considers pion-nucleon collisions to occur in a way similar to that involved in Fermi's statistical theory of meson production.[13] There is assumed to be a region of strong interaction about the nucleus with a radius of about 10^{-13} cm. Since λ (in the center of mass system) is about 3 x 10^{-14} cm, we may consider it either to hit this region and interact or miss it and fail to do so. If it hits, two or more pions may be emitted, in which case the process is obviously inelastic, or only one pion may emerge as an elastic scattering. In the latter case, the event should be counter as inelastic if the emitted pion is considered

to arise from a truly "thermal" process so that its phase is random with respect to the incoming pion and cannot interfere with it (incoherent elastic scattering). Fortunately the incoherent scattering should be isotropic if one thinks of it in terms of the thermal model, and thus it can easily be subtracted from the total elastic scattering. A more detailed description of diffraction scattering, which is described by the so-called optical model, will be found in Chapter VII.

Curves which show the proton-proton total cross section, elastic cross section, inelastic cross section and elastic differential cross section as a function of energy, will be found in Figures 2 and 3. As the bombarding energy is increased above the threshold for meson production (290 Mev) to about 800 Mev, the inelastic p-p scattering cross section rises, while the elastic cross section remains nearly constant. Thus, the rise in total cross section for p-p interactions occurring between 0.4 and 0.8 Bev is due to inelastic events leading to the production of one or more pions, the cross section for such processes being about 26 millibarns for energies from 0.8 to 6 Bev. In this energy range, the elastic cross section apparently drops slowly with increasing energy. The angular distribution, nearly isotropic at energies below about 400 Mev, exhibits an increasingly forward peaking as the bombarding energy increases, which reflects the inelastic processes that occur within a region larger than the wave length of the colliding particles. The low energy data can be described by a phase shift analysis. The high energy elastic proton-proton scattering is at least partly a diffraction effect arising from the inelastic processes that can occur. The small angle scattering can be fit by a variety of optical models.[14,15]
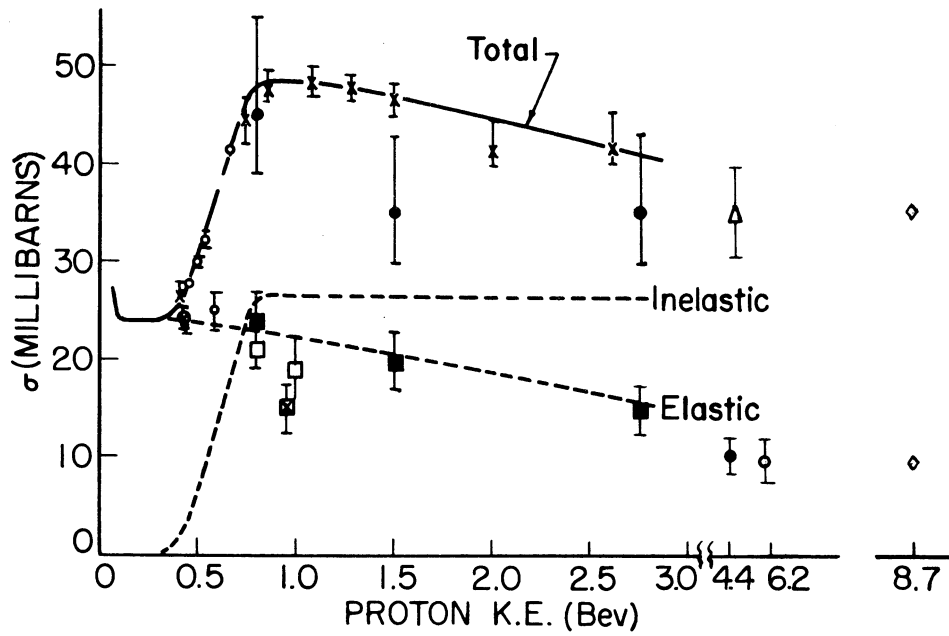
Figure 2. Total, Elastic and Inelastic p-p Cross Sections.
(For experimental points see References 14, 15.)
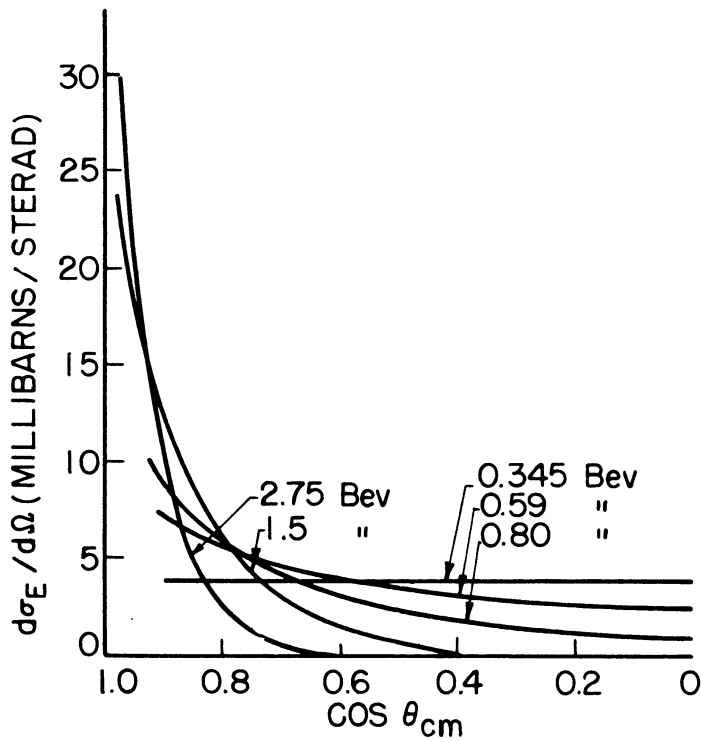
Figure 3. Elastic Differential Cross Sections for Incident
Proton Energies from 0.345 to 2.7 Bev (For experi-
mental points see Reference 14.)

Since the experimental p-p differential cross section decreases rapidly

with increasing scattering angle and apparently goes to zero for large

angles, the p-p elastic scattering, in contrast to the π^--p elastic

scattering, must include only a very small amount of incoherent scat-

tering.

2. Summary of Known Experimental Data

At the present, the total π^--p cross section is roughly known

to 5 Bev.[5-12] The elastic π^--p cross section is also known for this

same energy region.[5-12,28] (See Figure 1 and Table I.) It can be

seen that there are some large energy gaps in this range, however,

which should be removed. Also, most of the elastic cross sections have

rather large statistical errors attached to them due to the small num-

ber of events observed. The π^+-p total cross section is known to 1.9

Bev. However, the highest energy π^+-p elastic cross section measured

to date is only at 480 Mev.[16] The primary reason for the lack of

high energy π^+ experimental data is the fact that if the proton beam of

the cosmotron or bevatron is allowed to strike a target inside the

evacuated doughnut, the magnetic field of the accelerator in this region

will tend to force particles with a positive charge into the center of

the machine or at least along the proton orbit in the doughnut. Par-

ticles that are produced at the target with a negative charge, however,

will be ejected by the magnetic field into the experimental area. It

has been possible to obtain π^+ mesons in the experimental area by placing

the target in an appropriate section of the evacuated doughnut, but in

all cases when this was done, the proton contamination of the π^+ beam

was very high. It was for this reason that high energy π^+ experiments were not feasible. Lately a high energy (3 Bev) external proton beam has been developed at the cosmotron. With the advent of this external beam it is now possible to place the pion producing target outside of the magnetic field of the accelerator and in an experimental area. A high energy positive pion experiment is now possible. The experimental data to be reported in this thesis were obtained by using the external proton beam, and it will be the first high energy (1.1 Bev) π^+-p elastic scattering ever reported. The greatest importance of the data will be the knowledge it will give theoreticians who are at present formulating new models of the pion nucleon interaction which consider the isotopic spin of the π^+-p system and the charge of the pion.

The elastic and total cross sections for proton-proton collisions are known to an energy as high as 9 Bev.[14,15,17-19,32] The same comment concerning the π^--p cross section holds here also. That is, there are few measurements in the high energy region, and the data have large statistical errors. The energy of the bombarding proton in this experiment is 580 Mev. Proton-proton elastic scatter has already been measured at 560 Mev and 590 Mev.[17,18] Both of these experiments were performed with counters. The value of the proton-proton data in this thesis is primarily to show the agreement between bubble chamber measurements and counter measurements at this energy. It is desirable to make this comparison because although a counter experiment is capable of great statistical accuracy, it is also subject to rather large systematic errors.

TABLE I
(Taken from Reference 32)

ELASTIC, σ_e, AND INELASTIC, σ_i, CROSS SECTIONS FOR π^--p INTERACTIONS

Energy in Bev	σ_e mb	σ_i mb	σ_i/σ_e
0.307	10 $\pm$ 1	19	1.9
0.45	13 $\pm$ 2	16.4	1.26
0.60	19 $\pm$ 2.5	17.0	0.9
0.75	20 $\pm$ 2.5	23.5	1.15
0.80	21 $\pm$ 1	32.4	1.54
0.95	19 $\pm$ 1	25.9	1.36
1.00	20 $\pm$ 2	26	1.3
1.3	10 $\pm$ 1.5	19	1.9
1.4	10 $\pm$ 2	24	2.4
4.7	6 $\pm$ 1.5	22	3.7

II. EXPERIMENTAL APPARATUS AND ARRANGEMENT

1. The Bubble Chamber

A bubble chamber was the detecting instrument used in this experiment.[20] The chamber was made of aluminum, was rectangular in shape and had a sensitive volume of 12 x 5 x 5 inches. The chamber was operated at 51.9°C with a pre-expansion pressure of 375-400 psi. The liquid used in this chamber was propane, which has a vapor pressure at this temperature of 280 psi. Expansion and recompression were carried out by air pressure applied behind a rubber diaphragm in the bottom of the chamber. The top of the diaphragm was in contact with the propane. The chamber was expanded by applying an electronic pulse to a 3/4-inch commercial three-way solenoid valve. This actuated a larger poppet valve to provide expansion. A schematic drawing of the bubble chamber and associated equipment is shown in Figures 4, 5 and 6. The chamber was so oriented that the incident beam traversed the long dimension of the chamber.

In order to reconstruct accurately an event in real space from measurements made on stereoscopic negatives, sets of fiducial marks in the form of crosses were deposited on the inner surfaces of the front and back windows. These fiducial marks were placed in a rectangular pattern with a spacing of 1.000 ± 0.001 cm. In order to insure uniformity of the pictures, the camera and chamber were mounted on a rigid steel I-beam frame. Separate strips of 70 mm film were used for the two stereo photographs. To insure constant image distance, the film was held flat by means of pressure plates and vacuum backs in the camera. A line source of light was provided for bright-field photography by

-11-
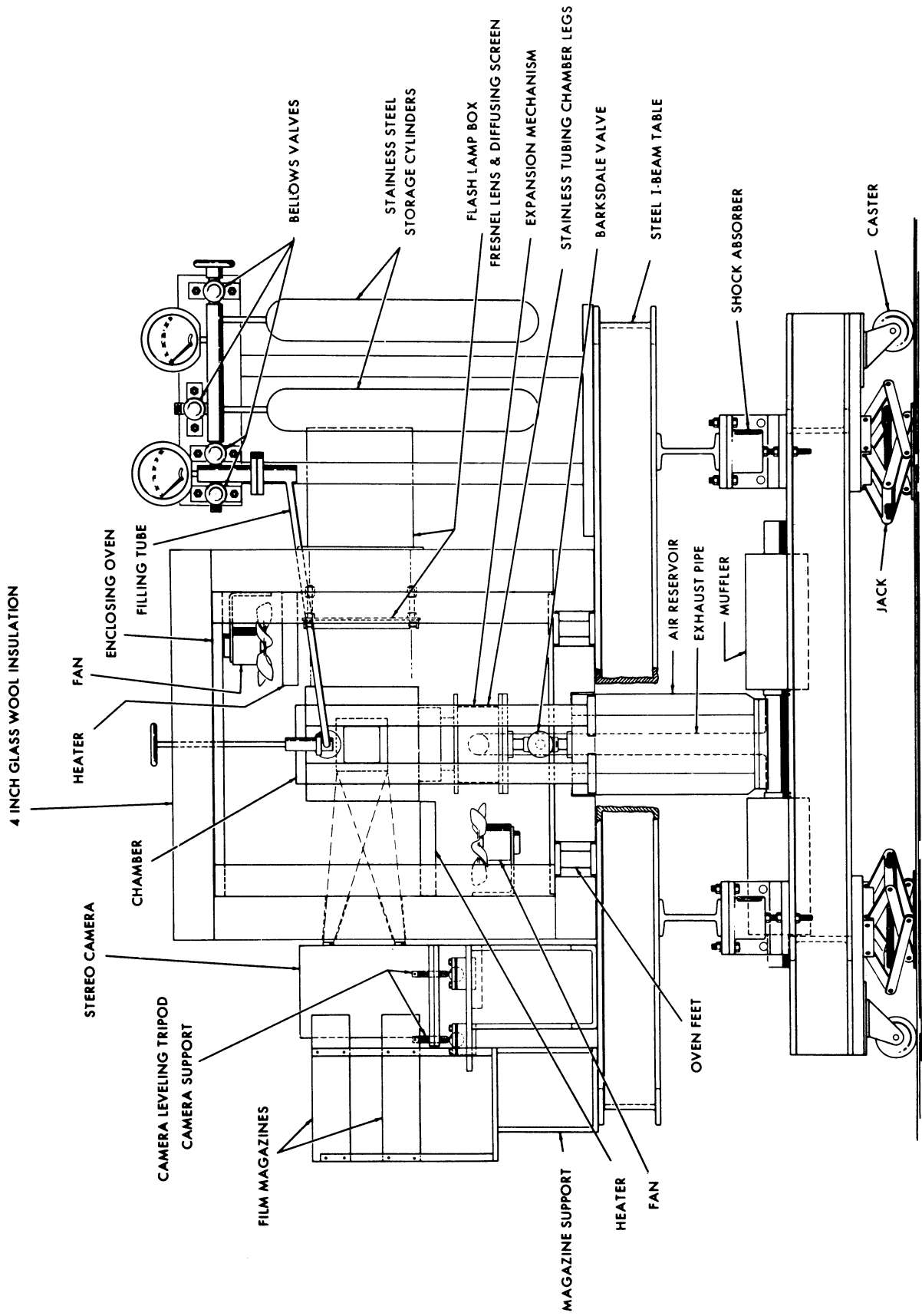
FIGURE 4. 12 INCH BUBBLE CHAMBER WITH STEREO CAMERA, OVEN, PLUMBING, AND SUPPORTING STRUCTURES.

1 -INCH TEMPERED GLASS WINDOW

TEFLON GASKET

RUBBER O-RING

BEAM "WINDOW"

COSMOTRON BEAM

TOP VIEW
OF
BUBBLE CHAMBER

WINDOW FRAME

WINDOW

THERMISTORS

THERMOCOUPLE

FILLING HOLE

CHAMBER BODY

SENSITIVE
VOLUME

EXPANSION THROAT

TEFLON
MYLAR
MYLAR
BUTYL RUBBER
TEFLON

DIAPHRAGMS

EXPANSION
VALVE

BUBBLE CHAMBER
AND
EXPANSION APPARATUS

PERFORATED PLATE

RUBBER O - RINGS

EXHAUST CHAMBER

BARKSDALE VALVE

TO MUFFLERS & EXHAUST SYSTEM

AIR RESERVOIR

THERMOCOUPLE

WINDING OF RESISTANCE
WIRE EXPANSION VALVE

AIR INPUT DISTRIBUTOR

CYLINDER OF 2 INCH INSULATION

AIR PREHEATER

COLD AIR INLET FROM COMPRESSOR

Figure 5. Detail Schematic Drawing of Chamber Proper.
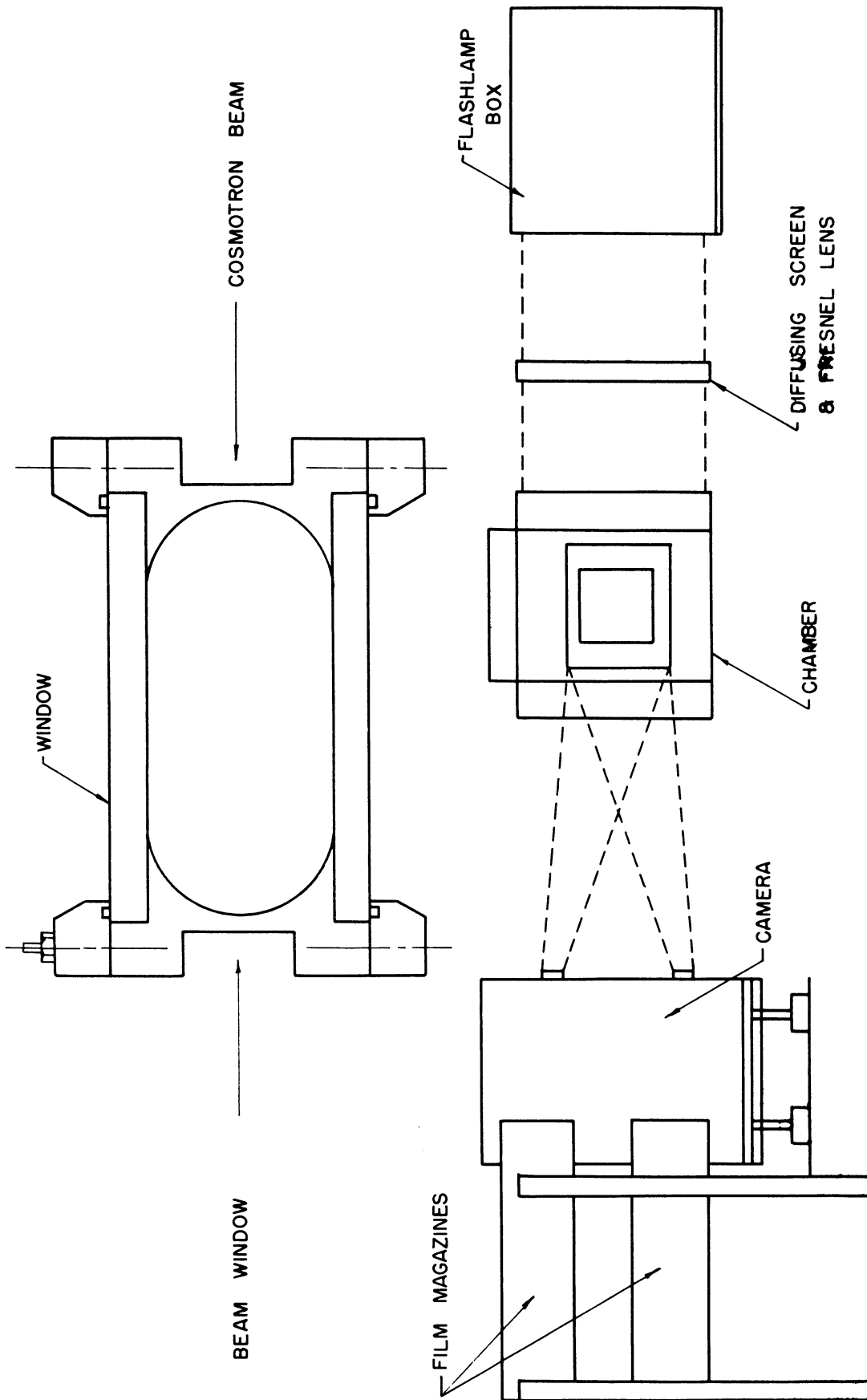
Figure 6. End and Top Views of Bubble Chamber.

means of two 6-inch xenon-filled flash tubes. The flash duration was about 40 microseconds and intense enough to allow the camera lens to be stopped down to f/45. This provided a depth of field sufficient to have all parts of the chamber in good focus. A fresnel lens and diffusing screen were employed to insure a uniformity of illumination throughout the chamber.

2. Experimental Arrangement

The experimental arrangement for this experiment was completely described in the doctoral thesis of J. C. Vander Velde, and the description given below closely parallels Vander Velde's description.[21]

A. The π^+ Beam

Early indications of the feasibility of obtaining a relatively pure π^+ beam from the cosmotron came from some pion-proton total cross section work done by Cool, et al.[3,23] This led to a further experimental study by Cool, Cronin and de Benedetti to determine the various proton-pion ratios possible as a function of pion momentum, production angle and target material. This work was carried out with the present bubble chamber experiment in mind, and the reader is referred to their paper[24] for a detailed description of the results. The essential features are as follows: The p/π ratio was found to decrease with decreasing atomic number of the target material and with decreasing pion momentum. This particular work was carried out at just one production angle (7°), but earlier results had indicated that the ratio would also decrease with decreasing production angle. For a desired pion momentum, therefore, one would like to use the lowest Z target and the smallest

production angle which is practical. In the course of one of these tests, our bubble chamber was placed in the beam in order to determine what the room background would be when the cosmotron intensity was such that an optimum number of particles per pulse passed through the chamber. It was found that the background was negligible, and it was concluded that a bubble chamber experiment to study the reactions $\pi^+ + P \rightarrow \Sigma^+ + K^+$, $\pi^+ + P \rightarrow \pi^+ + P$ and $P + P \rightarrow P + P$ was entirely possible.

B. The Beam Set-Up

We were led by this study to the experimental beam set-up which is described below. A pion laboratory kinetic energy of 1.1 Bev was chosen in order to afford a direct comparison of our results with those of a π^- experiment that had already been done at this energy in the same chamber. Figure 7 shows a floor drawing of the arrangement. The 3 Bev external proton beam strikes a 1 x 1 x 6 inch polyethylene target at T and produces a spectrum of pions in all directions. The high momentum mesons are produced most abundantly in the forward direction, so the strong focusing magnets H and J were set up to accept a solid angle centering around an angle of 7° with respect to the primary external beam direction. The acceptance angle was limited by the 3 x 3-inch collimator at (a), and that part of the primary beam which did not interact in the target was dissipated in the lead walls of this collimator and in the iron of the H magnet. The currents in the strong focusing lens were set so as to bring the image of the target to a focus at the one inch collimator (c). The magnet B deflected the beam through an angle of 23° and provided momentum analysis.

FIGURE 7. EXPERIMENTAL LAYOUT

B   Analyzing Magnet
E   Sweeping Magnet
H-J   Strong Focusing Magnets
a,b   3 inch Collimators
c   1 Inch Collimators
T   Polyethylene Target
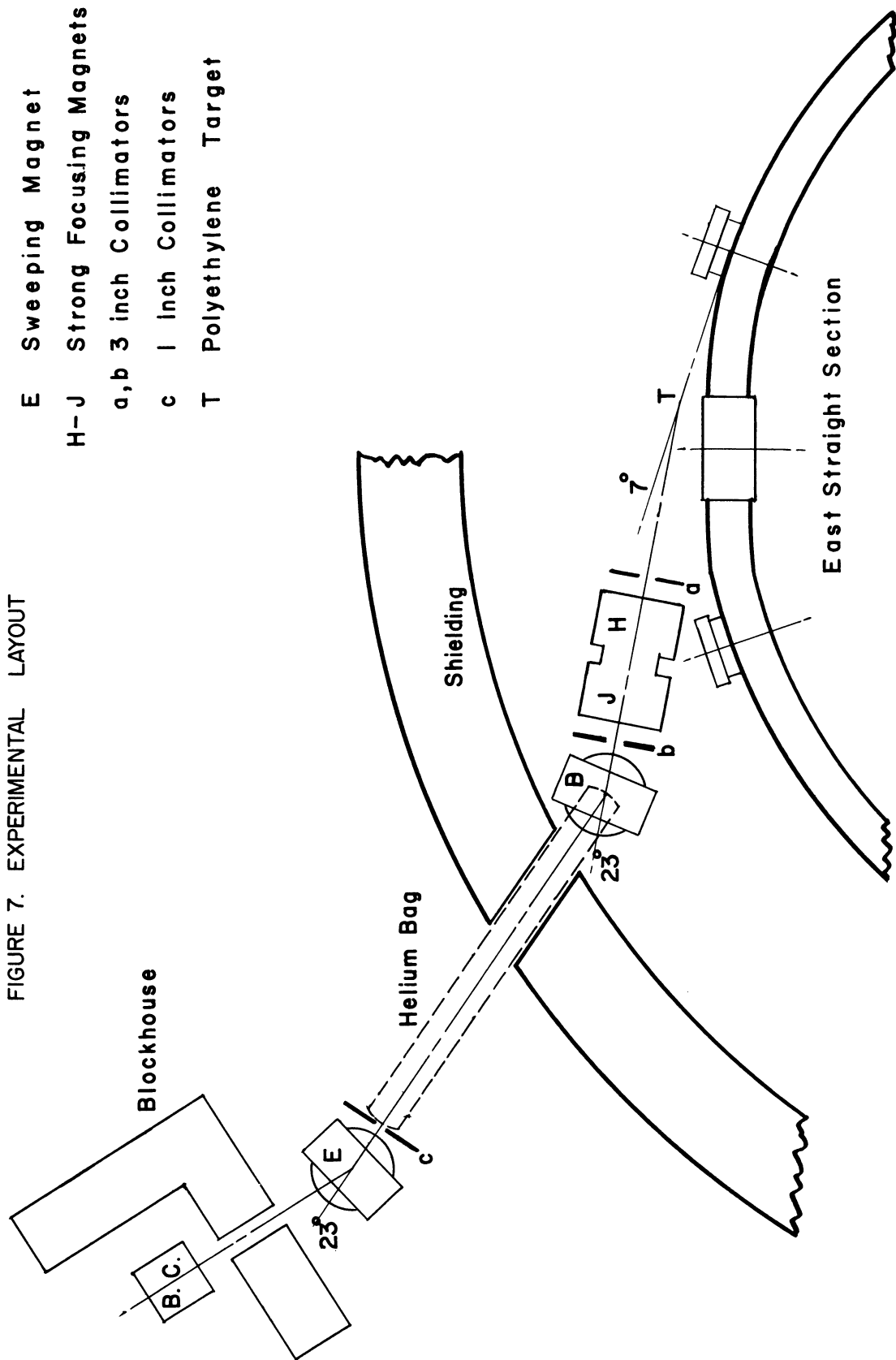
The expected momentum resolution for this set-up can be calculated from the relationship $\frac{\Delta P}{P} = - \frac{\Delta\Theta}{\Theta}$, where Θ is the angle of deflection and $\Delta\Theta$ is the differential angle of acceptance. In our case, $\Delta\Theta$ is proportional to the sum of the widths of the collimator (c) and that of the target image. From the known properties of the quadrupole lens[25] the target image was calculated to be 0.92 inches wide. This gives an expected resolution of $\pm$ 0.75%. It is desirable to have good resolution because the events are identified mainly on the basis of kinematics. As seen in the diagram, a plastic bag filled with helium was inserted between the magnet B and collimator (c). This was to reduce the broadening of the target image due to multiple air scattering, which would be appreciable at these distances.*[26] The magnet E did not provide any further momentum analysis, but served mainly to sweep out any low momentum particles which had lost energy in the collimation system. The beam then passed through the bubble chamber (B.C.) which was shielded from the general room background by a concrete blockhouse. After completing the initial set-up, it was necessary to perform a wire measurement on the system to insure proper alignment. A wire was suspended between the target and the chamber, and the current and tension adjusted so as to correspond to the desired momentum 1.232 Bev/c. Fine adjustments were then made so that the wire passed through the center of the collimators. The chamber was aligned so that the beam passed perpendicularly through the end of the chamber. A check was made of the chamber alignments and can be found in Figures 8 and 9.

---

* The r.m.s. deviation of a particle of our momentum passing through 30 feet of air would be about 1 cm. Helium reduces this by a factor of 30.

Figure 8. The Direction Cosine of the Beam Proton with Respect to the Y Axis for a Group of Scatterings.
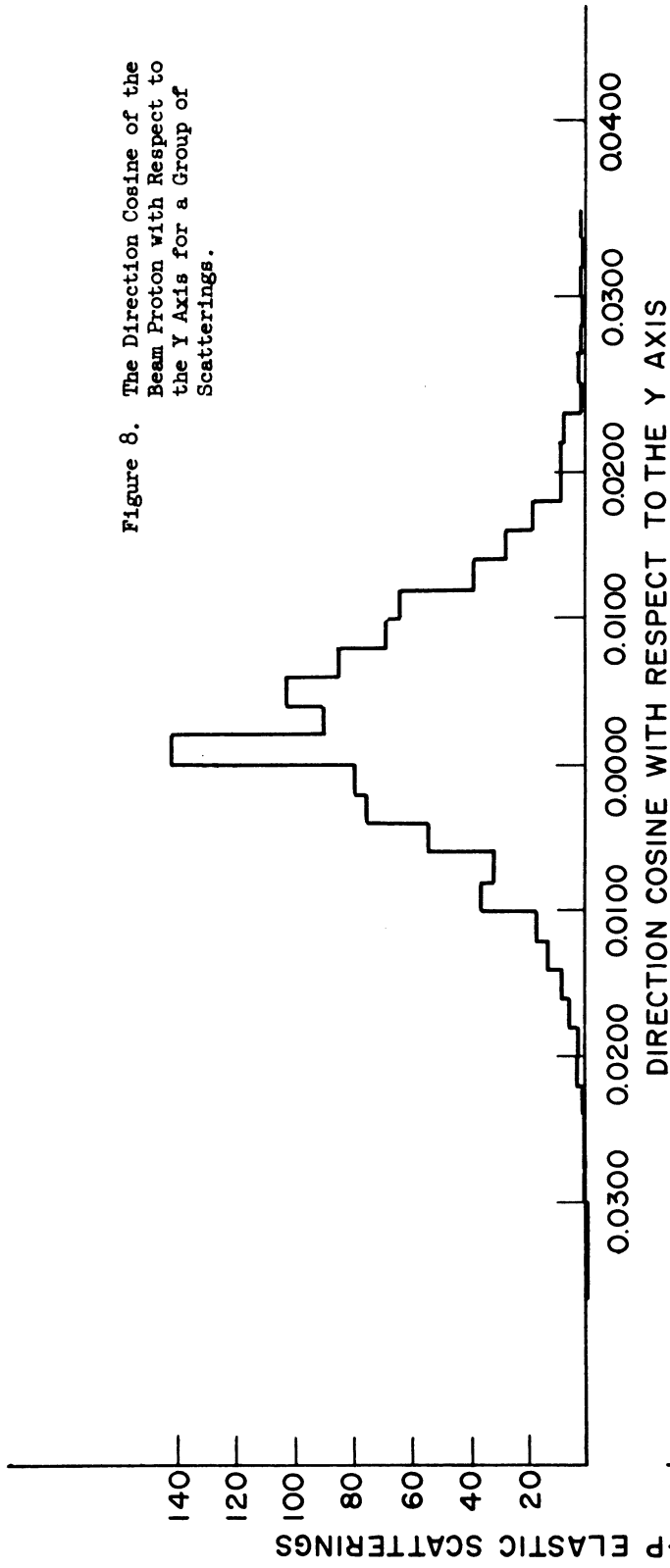
Figure 9. The Direction Cosine of the Beam Proton with Respect to the Z Axis for a Group of Scatterings.
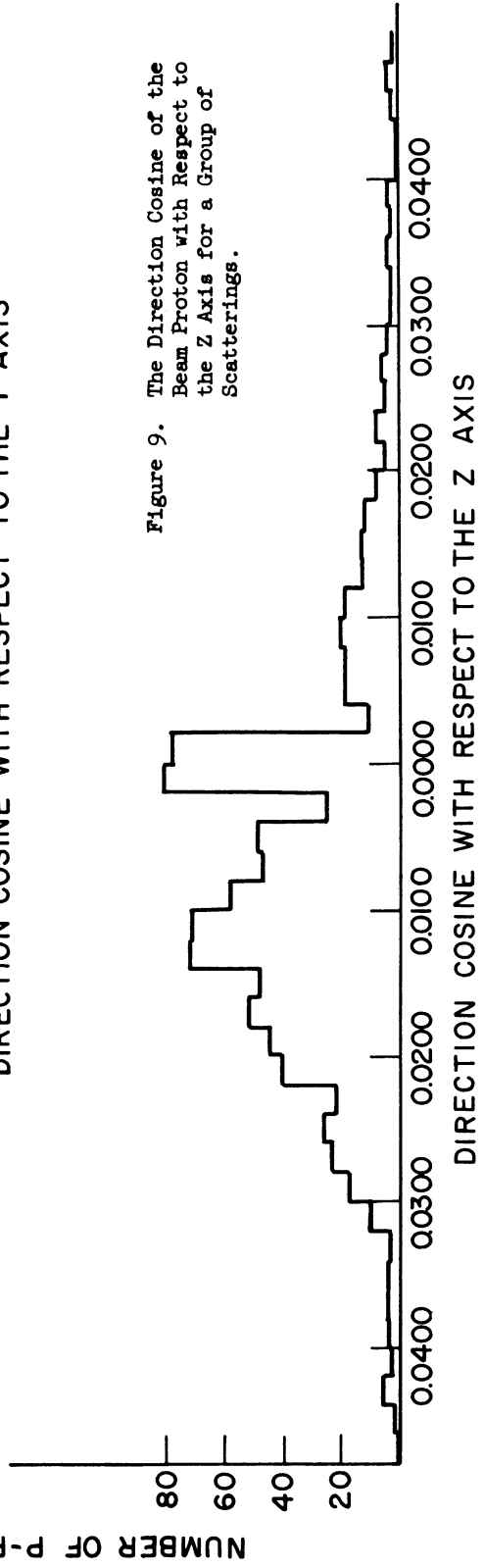
An important factor in the success of the experiment was the use of the rapid beam ejector developed at Brookhaven by D. C. Rahm.[27] This device reduces the duration of the beam pulses to a few microseconds, as opposed to a minimum of about two milliseconds without it. Because of the rapid bubble growth in propane, a two millisecond pulse will produce tracks which differ greatly in bubble size, whereas with the rapid beam ejector in operation they can be made uniformly small. This not only reduces measurement error, but in our case allowed us to have almost twice as many tracks per picture without affecting their ability to be scanned easily.

C. Counter Measurements

(1) Beam Width.--The sensitive volume of the bubble chamber is 5 x 5 x 12 inches, with the beam entering through the 5 x 5 inch cross section. Thus, it was desirable to have a beam which was somewhat narrower than five inches upon entering the chamber. This reduces the chances of losing sight of an interaction which occurs near the front or back window of the chamber and also reduces the background of stray particles which come from interactions in the glass or aluminum walls. The width of the beam at the chamber is determined by its angular divergence after passing through the focus at (c) and the additional spreading of the momentum components due to the sweeping magnet E. The collimation system was arranged so that an extreme-ray calculation gave a beam width of four inches for a beam with a momentum spread of $\pm$ 0.75%. Its height was also restricted to three inches by the three-inch-high collimators.

In order to check the beam width, a counter was moved laterally across the entrance side of the chamber and a plot made of intensity vs.

position. The curve showed a maximum at about 1/2 inch from the center of the chamber, and 95% of the beam fell within an interval of two inches on either side of this maximum. This agrees well with the 100% width of four inches that was calculated from the geometrical set-up and expected momentum spread and confirms the fact that the momentum resolution was $\pm$ 0.75%. However, variations which were observed in the analyzing magnet field must be independently added to this to give a final beam momentum of p = 1.232 Bev/c $\pm$ 1.5%. The expected width and height of the beam were also confirmed later by observation of the actual distribution of tracks in the pictures. See Figure 10 for the depth coordinate of the origin of 568 p-p elastic scatterings.

(2) <u>Proton to Pion Ratio</u>.--In order to calculate the cross sections for any observed processes, it is necessary to know the ratio of protons to pions which pass through the chamber. Actually, the beam contains not only p and π^+, but also a small contamination of μ^+ which must be taken into account. The pions and muons have practically the same velocity (β = 0.99), whereas the protons are significantly slower (β = 0.79) and can be separated electronically from the higher velocity component of the beam. A time-of-flight technique was used, similar to that of Cool, Piccioni and Clark.[3]

A counter telescope was placed in the beam with one pair of counters just outside the cosmotron shielding and the other pair immediately in front of the bubble chamber. The distance between the counters was 20 feet, which corresponds to a difference of 5.2×10^{-9} seconds between the flight times of the protons and mesons. The amount of delay necessary to bring the two pairs of counters into coincidence measures
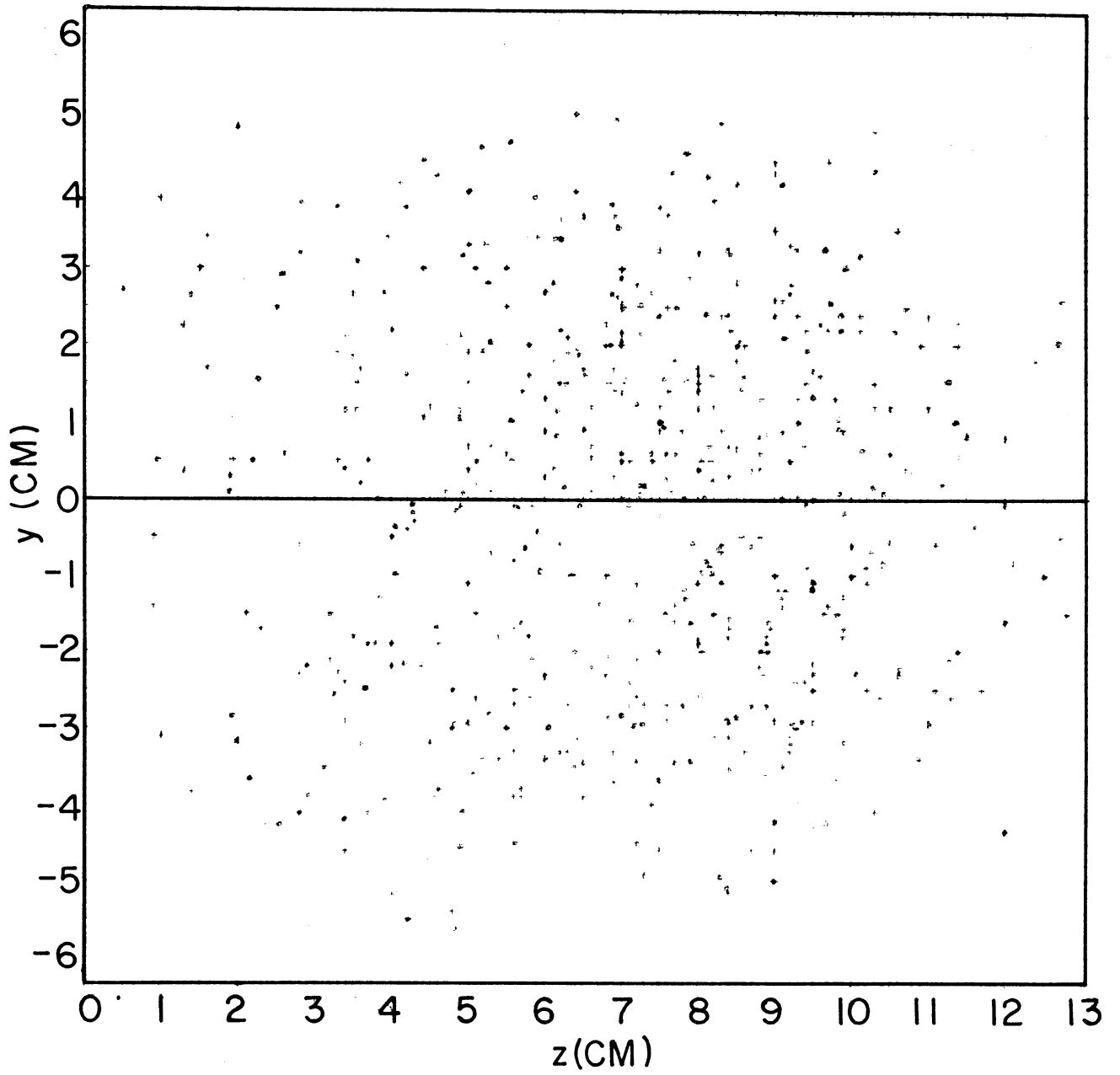
FIGURE 10

LOCATION OF 550 ELASTIC p-p SCATTERINGS

the flight time of the particles. Curves were plotted of intensity vs. delay time for both positive and negative beams of momentum 1.232 Bev/c. The intensity was normalized with a monitor counter and is plotted against the delay in feet of RG-63, as shown in Figure 11. The zero point of the abscissa was arbitrarily chosen to be at the center of the negative beam curve. Since the negative beam consists of pions and muons only, it gives the delay curve for a pure beam of $\beta = 0.99$ particles. Curve II is the one obtained for the positive beam and clearly shows the two velocity components. Since the width of the curves is due only to the pulse widths from the counters, it is the same for all velocity components, and the leading edge of Curve II can be assumed to be due solely to the high velocity component of the positive beam. Thus, the negative beam, Curve I, is normalized to follow this leading edge, and the difference between II and I gives the proton delay Curve III. This has the same shape as Curve I and is shifted by an amount corresponding to the predicted difference in flight time. The relative heights of Curves III and I then give the ratio of protons to pions and muons. This ratio is 1.75 $\pm$ 0.09. The errors quoted are due partly to statistics and partly to an uncertainty in normalizing Curve I to the leading edge of Curve II.

By previous measurements in similar beams[3], it was estimated that the muons represent a contamination of $(8 \pm 3)\%$ of the pions.
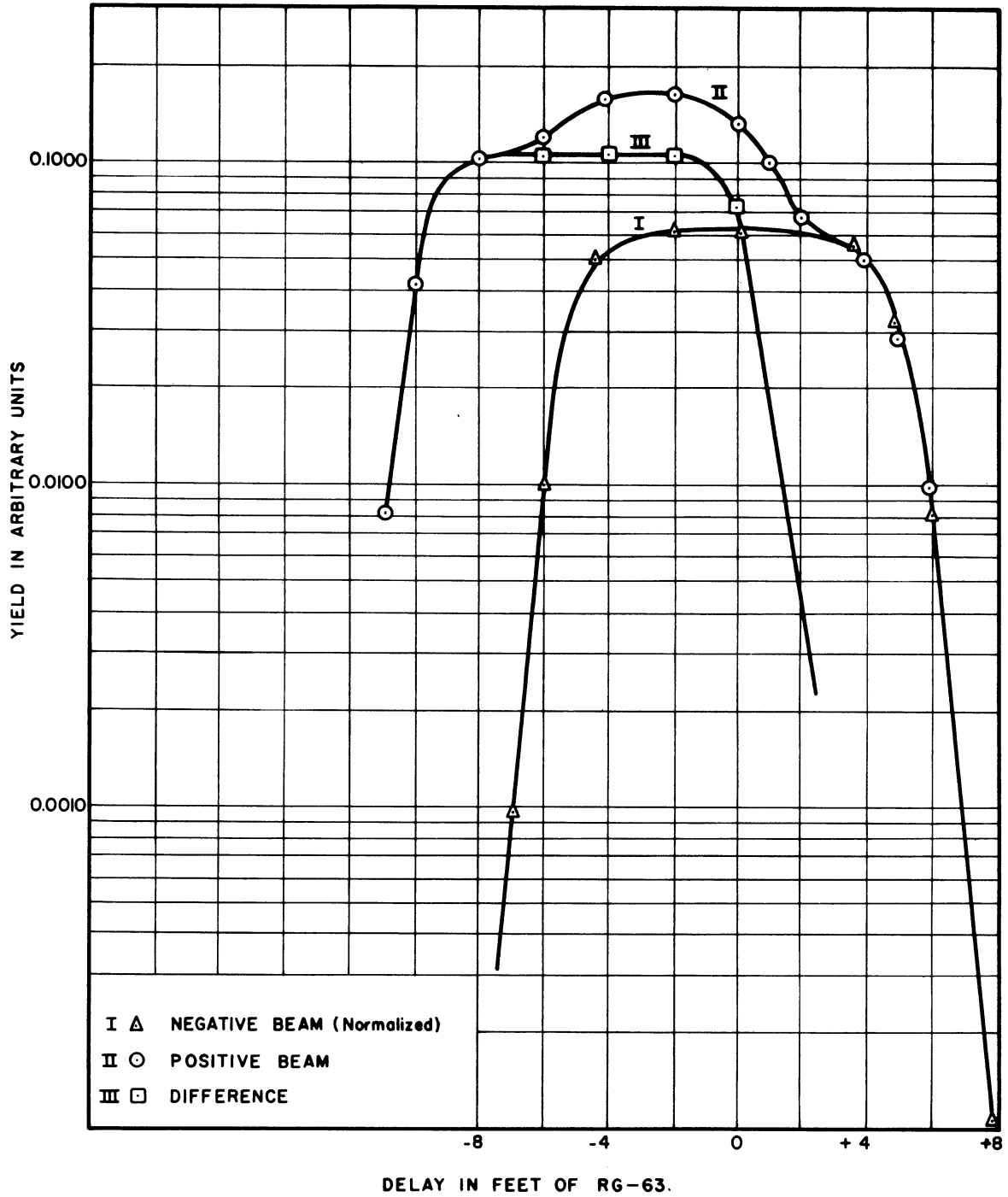
FIGURE II. DELAY CURVES

III. REDUCTION OF DATA

1. Scanning, Measurement and Computation

A total of 234,000 tracks was scanned for elastic scatterings
of positive pions and protons by free protons. Because these elastic
scatterings are two-body processes, the beam particle direction must be
contained in the plane of the V formed by the two particles after the
scattering has taken place, in order that transverse momentum be con-
served. The scanners were instructed to look for all Y-shaped events
in which the direction of the beam particle went through the two arms of
the V, and if these Y-shaped events (also called two-prong stars) were
produced by a beam particle, they were to measure them on the film.

The measurements were made with a 7-power Bausch & Lomb
measuring magnifier. The scale on the measuring magnifier was of special
design in order that rapid measurements could be made on the film. A
floating origin system was used for the measurements. As mentioned in
Chapter II, the windows of the bubble chamber were inscribed with small
crosses one centimeter apart which were to be used as fiducial marks.
These crosses served as axes for a cartesian coordinate system. Hori-
zontal and vertical measurements were made from nearest set of available
axes (occasionally beam tracks would obscure a fiducial mark) to the
bubble which was to be measured. The horizontal and vertical measure-
ments were read on the scale to within 0.005 cm. The set of axes was
chosen so that measurements were always made in the positive quarter
plane. Each cross was given a code number so that the set of axes which
was used for the measurements could be identified.

The Y-shaped events that were to be measured were divided into three categories. The first category included all of the events in which the two scattered particles left the chamber. For this case, a measurement was made as far out on the arms of the Y as possible, in order to obtain the greatest possible angular accuracy. There were two cases in this category when it might not be possible to measure the arms a long distance from the origin of the scattering. The first was when the scattered particle underwent some sort of nuclear reaction, and second when the scattered particle had its direction altered appreciably by coulomb scattering. For these cases, the length 2-3 or 2-4 might be quite small, see Figure 12. The second category included all events in which one or both scattered particles appeared to stop in the chamber. In this case, the end of the track was measured to obtain the range of the particle if it stopped in the chamber, or to find out if the particle went out the front or rear glass window of the bubble chamber, for particles that go out either of the windows have the appearance on the film of stopping in the chamber. In these cases, by looking at the depth coordinate it was possible to ascertain if it did go out one of the windows. The third category consisted of those events which scatter slightly before they appear to end. In this case, a measurement was made along the arm before the second scattering to obtain angular accuracy, and then a measurement was made at the end of the particle to find out if the particle went out through a window, and if it did not, to obtain its range. To help eliminate Y's which had short arms due to the fact that the scattering took place near one of the ends of the chamber, the only scatterings that were measured were those in which the center of the scattering took place in the middle two-thirds of the chamber.
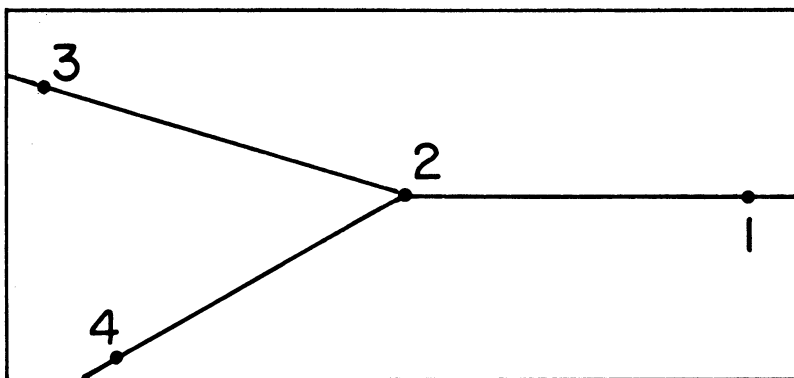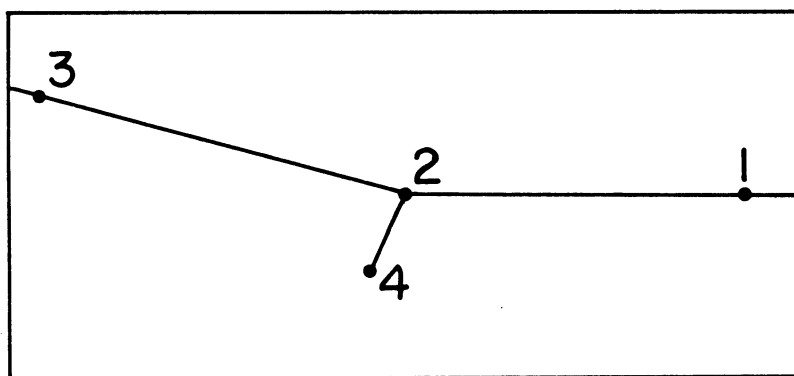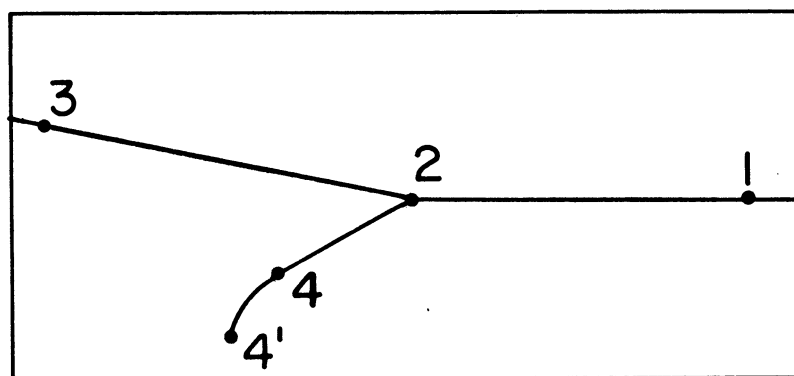
Figure 12. Three Types of Scatterings.

The measurements that were made by the scanners were then punched on IBM cards which were fed into an IBM 650 computer. The computer calculated the following physical quantities of the event: the real space coordinates of points 1, 2, 3 and 4; the direction cosines of the incoming beam track, the direction cosines of the normal to the scattering plane (from this the azimuthal angle of the scattering can be calculated); the lengths ℓ_{12}, ℓ_{23} and ℓ_{24}, the coplanarity angle, ϕ, (the angle between the beam track and the scattering plane); the two scattering angles θ_1 and θ_2; and a geometric error to be assigned to the lengths ℓ_{12}, ℓ_{23}, ℓ_{24} and the angles ϕ, θ_1 and θ_2.

2. Errors

The geometrical error mentioned above is an error that is caused by the geometry of the event, i.e., it is a measure of the variations in the computed physical quantities caused by a slight (slight is defined below) variation in the measurements of the points on the film. For example, if one or more of the arms of the event is short, a given variation in the measurement of points on the event would correspond to a larger computed angular variation than if all the arms were relatively long. Another source of error results from the fact that an examination of the stereographic reduction formulas, which convert the measurements taken on the two stereographic film negatives to real space coordinates, shows that for a given variation on the film measurements, the variation in the real Z (depth) coordinate is eight times as great as it is for the real X and Y coordinates. Thus, for an event in which the scattering plane is parallel to the plane of the windows of the bubble chamber, a given measurement variation would cause a large variation in the

coplanarity angle, ϕ , and a small variation in θ_1 and θ_2. If the scattering plane were perpendicular to the plane of the window, the reverse would be true. As an indication of the errors that must be attached to the computed quantities, a well-known equation of statistics was used:

$$\Delta f = \left[\sum_{i=1}^{N} \left(\frac{\partial f}{\partial \chi_i} \Delta \chi_i \right)^2 \right]^{1/2} \qquad (1)$$

where Δf is the deviation of the function f in terms of the independent deviations $\Delta \chi_i$ of the N independent variables χ_i. Thus, if $\Delta \chi_i$ is the standard deviation of a measured quantity, then Δ f is the standard deviation of the function. If $\Delta \chi_i$ is an average deviation, then Δ f is also an average deviation. Now to measure a point on a scattering three independent measurements must be made on the stereographic film. Since a scattering is determined by four points, there is a total of twelve independent measurements for each event. Let $\Delta \chi_i$ i = 1,2,3, ...12 be the amount of measurement error in determining each coordinate. Then the function f can be any one of the computed quantities ϕ , θ_1, θ_2, ℓ_{12}, ℓ_{23} or ℓ_{24}. The measurement error $\Delta \chi_i$ was taken to be 0.005 cm, which was the smallest unit of measurement that was used. This value was chosen by the author after he made many measurements.

To test this hypothesis, 24 independent measurements were made on a single event by the scanners. Each scanner made the series of measurements more than once, but in each case there was a three- to four-day time elapse between the series of measurements so that each series of measurements would be independent. The results of this test

are given in Table II. A, B, C and D refer to the scanners. The sub-scripts refer to their first, second or third time for the measurements. The first measurements of Scanner A (who was considered one of the best measurers) were taken as the base. The deviations from her first measurements are shown in the table.

Using the definition of a partial derivative

$$\frac{\partial f}{\partial x_1} = \lim_{\Delta x_1 \to 0} \frac{f(x_1 + \Delta x_1, x_2, x_3 \cdots x_{12}) - f(x_1, x_2, x_3 \cdots x_{12})}{\Delta x_1}$$

Expression (1) can be written

$$\Delta f = \sqrt{\left[f(x_1 + \Delta x_1, x_2, \cdots x_{12}) - f(x_1, x_2, \cdots x_{12}) \right]^2 + \cdots}$$
$$+ \left[f(x_1, x_2, \cdots x_{12} + \Delta x_{12}) - f(x_1, x_2, \cdots x_{12}) \right]^2$$

This expression, computed for each event, was used to assign a geometrical error to the lengths ℓ_{12}, ℓ_{23}, ℓ_{34} and the angles ϕ, θ_1 and θ_2.

TABLE II

RESULTS OF THE MEASUREMENT ERROR TEST

Point Measured	SCANNER								
	A_1	A_2	B_1	B_2	C_1	C_2	D_1	D_2	D_3
V_1	0.000 cm.	0.000 cm.	0.000 cm.	0.000 cm.	0.005 cm.	0.000 cm.	0.000 cm.	0.000 cm.	0.000 cm.
W_1	0.000	0.000	0.005	0.000	0.000	0.000	0.000	0.000	0.000
U_2	0.000	0.000	0.000	0.000	0.005	0.005	-0.005	0.000	-0.005
V_2	0.000	0.000	0.000	0.000	0.000	0.000	0.000	0.000	0.000
W_2	0.000	0.000	0.000	0.000	0.000	0.000	0.005	0.000	0.000
V_3	0.000	0.000	-0.005	-0.005	-0.005	0.005	-0.005	0.000	-0.005
W_3	0.000	-0.005	-0.005	0.000	-0.005	-0.005	-0.005	-0.005	-0.005
V_4	0.000	0.000	0.000	0.000	0.000	0.005	0.000	0.000	0.000
W_4	0.000	0.000	0.000	0.000	0.000	0.005	0.000	0.000	-0.005
V_5	0.000	0.000	0.000	0.000	0.000	0.000	0.000	0.000	0.000
W_5	0.000	0.000	0.000	0.005	0.000	0.000	0.000	0.000	0.000
V_6	0.000	0.005	0.000	0.000	0.005	0.000	0.000	0.000	0.000
W_6	0.000	0.000	0.000	0.000	0.000	0.000	-0.005	0.000	0.000
V_7	0.000	0.000	0.005	0.005	0.005	0.005	0.005	0.000	0.005
W_7	0.000	0.000	0.000	0.000	0.005	0.005	0.000	0.000	0.000
V_8	0.000	0.000	0.000	0.000	0.000	0.000	0.000	0.000	0.000
W_8	0.000	0.000	0.000	0.000	0.000	0.000	0.000	0.000	0.005

IV. IDENTIFICATION OF ELASTIC SCATTERINGS

Elastic π^+-p and p-p scatterings were identified by the fol-
lowing methods: angular correlation, coplanarity, range, bubble density,
and δ rays produced by the beam track. Before a measured two-prong
star was classified as a π^+-p or p-p elastic scattering, the first four
criteria -- angular correlation, coplanarity, range and bubble density --
had to be satisfied. The last criterion, the use of δ rays, was used
only when the first four methods were not able to distinguish between
an elastic π^+-p scattering and an elastic p-p scattering. Measured
two-prong stars which were not classified as elastic scatterings were
either π^0 production produced by the incoming beam impinging upon a
free proton (the hydrogen atoms in the propane molecule) or the interac-
tion of the beam particle with a carbon atom in the propane molecule.
The following reactions are among those which would produce a non-elas-
tic event that would have two out-going prongs:

$$\pi^+ + p \rightarrow \pi^+ + p + n\,\pi^0 \qquad\qquad P + P \rightarrow P + P + n\,\pi^0$$

$$\pi^+ + C \rightarrow \pi^+ + B + P + n_1 N + n_2\,\pi^0 \qquad P + C \rightarrow P + P + B + n_1 N + n_2\,\pi^0$$
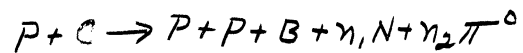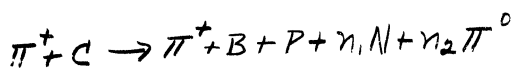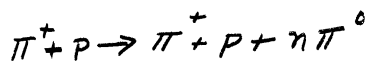
Below is a discussion of each of the five methods for identi-
fying a measured two-prong star.

1. Angular Correlation

The kinematic restriction for the reaction A + B → A' + B'
can be represented by a curve which is plotted by using $\Theta_{A'}$ and $\Theta_{B'}$ as
the coordinates where $\Theta_{A'}$ and $\Theta_{B'}$ are the laboratory angles of the two
outgoing particles A' and B' with respect to the incident direction of

particle A. These curves are based on the requirement of conservation of energy and momentum. The form of the curve is governed by the masses and energies of the particles involved. In Figure 13 is shown the kinematic curves for the reactions $\pi^+ + p \rightarrow \pi^+ + p$ and $p + p \rightarrow p + p$.

It is to be noticed that for small angle scatterings it is not possible to distinguish a $\pi^+ - p$ elastic scattering from a p-p elastic scattering. Because each event has its own peculiar geometrical error, it is not possible to state in general how small the angle of a scattering can be and still allow a $\pi^+ - p$ event to be distinguished from a p-p event. The lower limit is usually about 17°.

2. Coplanarity

Conservation of momentum demands that the track produced by the incoming beam particle lie in the same plane as that defined by the two outgoing tracks. The degree of non-coplanarity of an event is measured by the angle that the beam track makes with the scattering plane. For an event which is perfectly coplanar, this angle ϕ would be 0 degrees. In Figure 14 is shown a histogram of the coplanarity of 568 accepted elastic scatterings and the coplanarity of the rejected two-prong stars. The shape of the accepted elastic curve resembles a gaussian with a narrow half width as is to be expected. For the rejected events one expects a rather broad distribution inasmuch as these events consist of inelastic $\pi^+ - p$, $\pi^+ - c$, p-p and p-c interactions. The coplanarity of these events, however, is still peaked around small angles because of the high energy of the incoming beam. As mentioned in Chapter III, the geometrical error in the coplanarity angle is at a maximum when the scattering plane is parallel to the plane of the
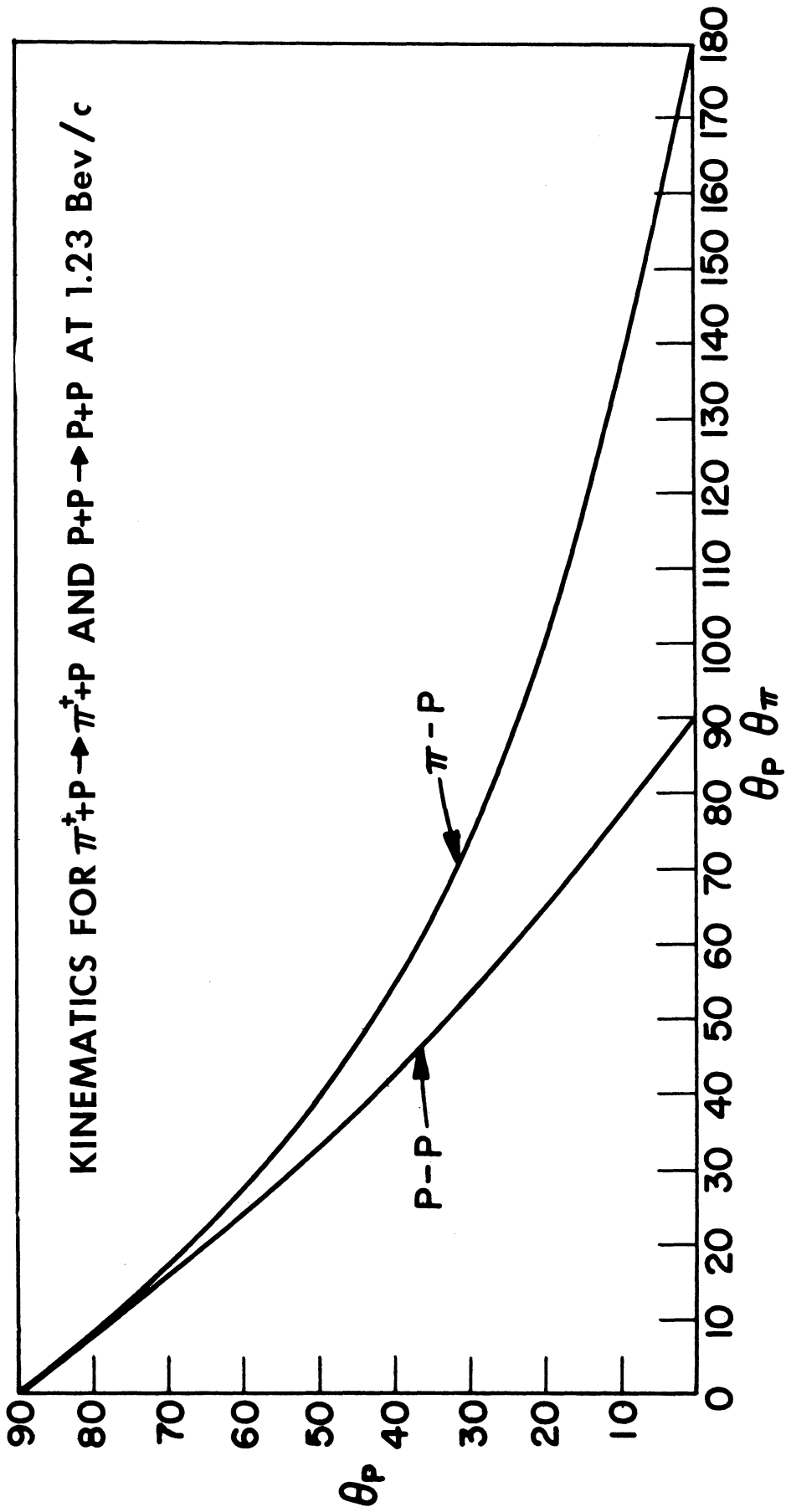
Figure 13. Kinematics for $\pi^+ + p \rightarrow \pi^+ + p$ and $p + p \rightarrow p + p$ at 1.23 Bev/c.
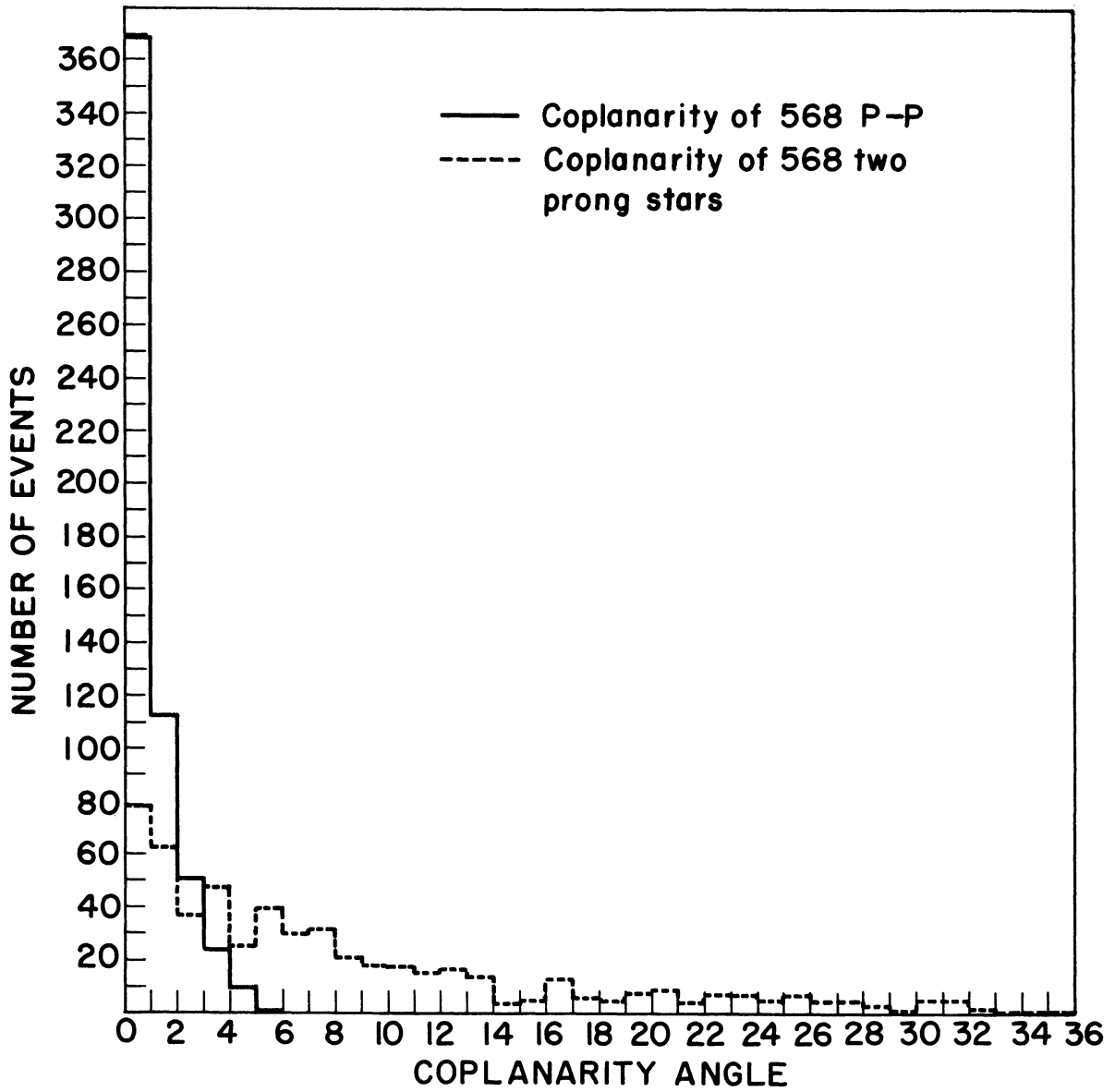
Figure 14. Coplanarity Histogram.

window, and the angular geometrical error is at a minimum in this case.
It was also noted that when the scattering plane is perpendicular to the
glass windows, the reverse is true. Thus, it is rather fortunate that
criterion 1 becomes more reliable where criterion 2 is weak and vice
versa.

3. Range

The range of a particle which stops in liquid propane can be
related to the energy that the particle possessed at the point of the
scattering. This, in turn, can be related to the scattering angle by
use of kinematics, and a correlation can be made between the angle at
which the particle comes off and its range in propane. This correla-
tion is shown in Figure 15. On the abscissa is plotted the angle of the
proton for π^+-p and p-p elastic scatterings, and on the ordinate is
plotted the range of the proton in the bubble chamber. Although this
criterion is sensitive for distinguishing elastic events from inelastic
events, it loses its usefulness for separating elastic π^+-p scatterings
from elastic p-p scatterings for small angle scattering, i.e., when Θ p
is large.

4. Bubble Density

The usefulness of the bubble chamber as a detection device is
enhanced by the experimental finding that the density of bubbles along
a track is a quantitative measure of the velocity of charged parti-
cles.[29] For a given scattering the velocities of the particles in-
volved can be computed by the use of kinematics, and thus, the bubble
densities of the tracks can be predicted. For this experiment, bubble
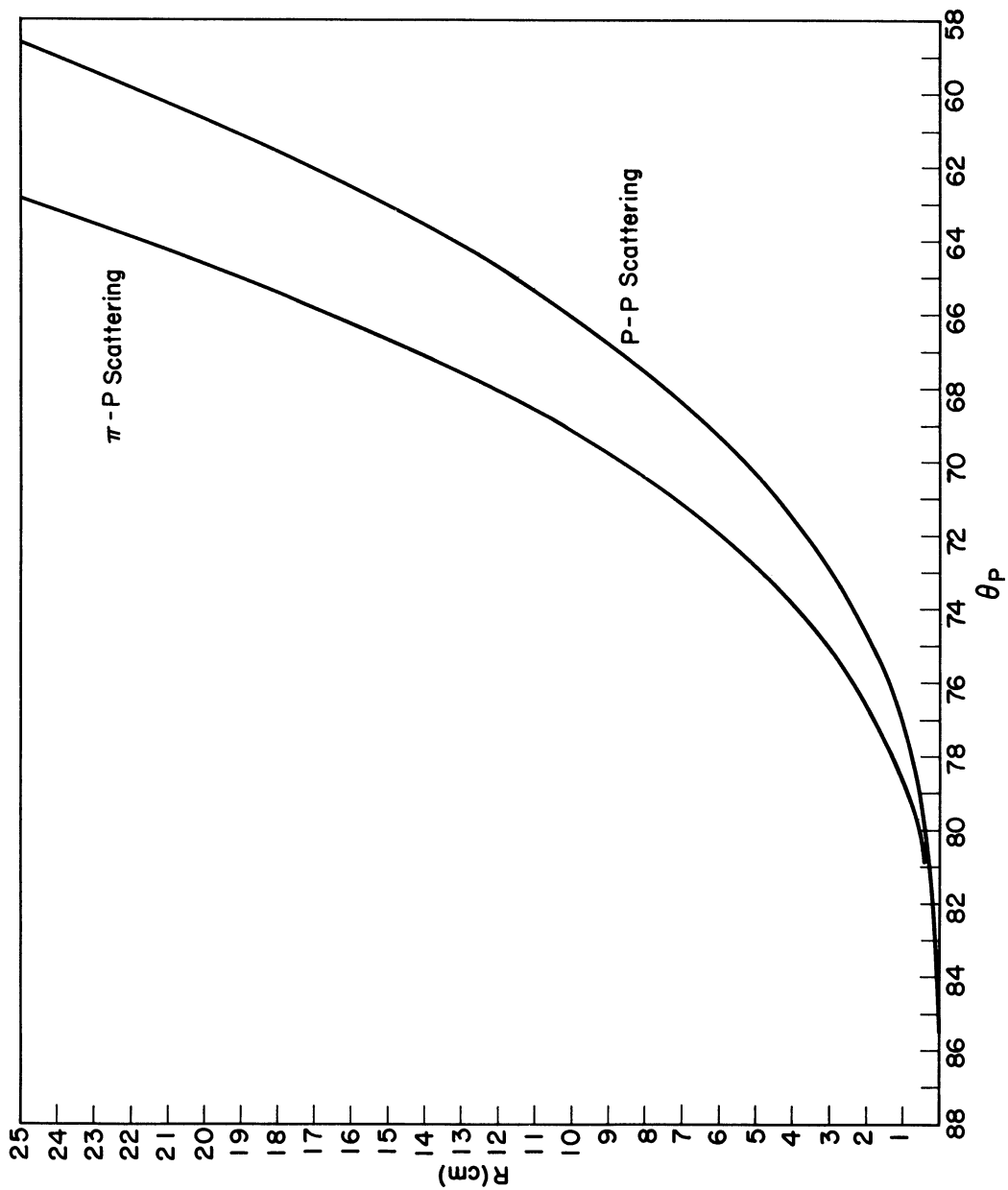
FIGURE 15. THE RANGE OF THE PROTON FOR π^+-P AND P-P
SCATTERINGS AT 1.23 BEV/C AS A FUNCTION
OF THE PROTON ANGLE.

density was not used in the quantitative sense. If it were to be used

quantitatively, various factors which could alter the bubble density on

the film would have to be computed for each event. These factors include

the change in demagnification of the track depending upon its depth in

the chamber, the foreshortening of the projected length of track, and

hence, the increase in bubble density because the azimuthal angle is

large, etc. Instead bubble density was used in a qualitative sense.

The bubble density of tracks was classified as being light, medium,

dense or very dense. Before an apparent elastic scattering could be

classified as a true elastic scattering, the bubble density of the event

was compared with the bubble density which was calculated for the event.

This criterion was especially useful in rejecting apparent π^+-p scatter-

ings, for at all angles of scattering (including directly backwards,

i.e., $\Theta_\pi = 180°$) the pion track must be light. About 10% of the appar-

ent π^+-p scatterings were rejected because the pion track was not light.

5. δ Rays
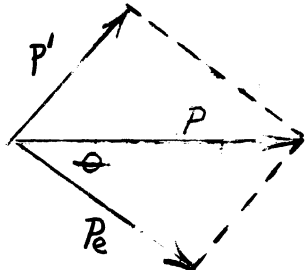
δ rays produced by the beam particles were used to differen-

tiate π^+-p elastic scatterings from p-p elastic scatterings when the

above four criteria were unable to do this. As mentioned above, for

small angle scatterings it was not possible to distinguish π^+-p elas-

tic scatterings from p-p elastic scatterings. There were also cases when

Θp or Θ_π was greater than 17° when it was not possible to separate these

events. This occurred when the scattering had a peculiar geometry which

could cause a large angular error, e.g., in the case where the scattered

particle would be scattered a second time close to the vertex of the

first scattering. In these cases, the measureable track length of the

scattered particle is short, and hence the error in the angular

measurement could be large.

The use of δ rays to distinguish π beam tracks from p beam

tracks is based upon the fact that for a given momentum a π meson can

impart more energy to a struck electron than a proton can. This can

easily be seen by applying the laws of conservation of energy and mo-

mentum to the case of a particle of mass m possessing a momentum P

striking an electron of mass m_e which is at rest and imparting a kinetic

energy E_e and a momentum P_e to the electron. The principle of conser-

vation of energy gives

$$\sqrt{P^2 c^2 + m^2 c^4} + m_e c^2 =$$

$$\sqrt{P'^2 c^2 + m^2 c^4} + E_e + m_e c^2 \tag{4}$$

The conservation of momentum gives

$$P'^2 = P_e^2 + P^2 - 2 P P_e \cos \theta \tag{5}$$

where P' is the momentum of the particle of mass m after the collision

with the electron. Elimination of P' between (4) and (5) yields:

$$E_e = 2 m_e c^2 \frac{P^2 c^2 \cos^2 \theta}{\left[m_e c^2 + (P^2 c^2 + m^2 c^4)^{1/2} \right]^2 - P^2 c^2 \cos \theta} \tag{6}$$

The maximum transferable energy corresponds to a "head-on" collision and has the value:

$$E_{e_{max}} = 2 m_e c^2 \frac{p^2 c^2}{m_e^2 c^4 + m^2 c^4 + 2 m_e c^2 \left(p^2 c^2 + m^2 c^4\right)^{1/2}} \qquad (7)$$

From Equation (7) it can be calculated that the maximum energy a 1.19 Bev/c proton can give an electron is 1.66 Mev, whereas the maximum energy a 1.23 Bev/c pion can give an electron is 74.5 Mev.

Bhabha has calculated the collision probability, $\Phi(E, E_e) dE_e dx$ for a charged particle of mass m and spin 0 of kinetic energy E, traversing a thickness dx gm cm^{-2}, to transfer an energy between E_e and $E_e + dE_e$ to an atomic electron.[30] His expression is:

$$\Phi(E, E_e) dE_e = \frac{2 C m_e c^2}{\beta^2} \frac{dE_e}{(E_e)^2} \left[1 - \beta^2 \frac{E_e}{E_{e_{max}}} \right] \qquad (8)$$

$$C = \pi N \frac{Z}{A} r_e^2 = 0.150 \frac{Z}{A} \text{ gm}^{-1} \text{ cm}^2$$

where Z and A are the charge and mass number of the material, N is Avagadro's number and $\Gamma = \frac{e^2}{m_e c^2}$ is the classical radius of the electron. β equals the velocity of the particle of mass m and spin 0 divided by the velocity of light.

To find the probability, Φ, that a 1.23 Bev/c pion produces a δ ray with energy between E_e and E_e $_{max}$ we integrate Expression (8)

$$\Phi = \int_{E_e}^{E_{e_{max}}} \Phi(E, E_e) dE_e = \frac{2 C m_e c^2}{\beta^2} \left[\int_{E_e}^{E_{e_{max}}} \frac{dE_e}{E_e^2} - \frac{\beta^2}{E_{e_{max}}} \int_{E_e}^{E_{e_{max}}} \frac{dE_e}{E_e} \right]$$

$$= \frac{2 C m_e c^2}{\beta^2} \frac{1}{E_e} \left\{ 1 - \frac{E_e}{E_{e_{max}}} \left[1 + \beta^2 \ln \frac{E_{e_{max}}}{E_e} \right] \right\} \qquad (9)$$

Now the probability Φ of a certain interaction measured in $cm^2 gm^{-1}$ is related to the molecular cross section, σ, for the same interaction measured in cm^2 by the equation $\Phi = \dfrac{N\sigma}{A}$. Letting E_e equal the maximum energy a beam proton can give an electron, 1.66 Mev, and $E_{e\ max}$ equal the maximum energy a beam pion can give an electron, 74.5 Mev, it is found that the cross section for a pion to produce a δ ray with 1.66 Mev $\leq E_e \leq$ 74.5 Mev in propane is 3.62×10^{-24} cm^2.

By scanning the beam tracks which terminate in an elastic scattering which fell into the unknown category and counting those δ rays produced along this track before the scattering occurred which had an energy greater than 1.66 Mev, it was possible to calculate the total length of pion track scanned by using the above cross section for high energy δ ray production. If the mean free path for the beam protons and pions is long with respect to the length of the bubble chamber, then

$$\frac{n_\pi}{n_T} = \frac{\ell_\pi}{\ell_T}$$

where n_π = number of pions in the group of unknown elastic scatterings,

n_T = total number of unknown elastic scatterings,

ℓ_π = calculated length of pion track scanned based upon the number of δ rays found,

and ℓ_T = total length of beam track scanned which terminated in an unknown elastic scattering.

A total of 4.73×10^6 cm of track was scanned. There were found to be 9,800 two-prong events which fulfilled the criteria outlined in Chapter II. These were measured, computed and analyzed using the first four criteria mentioned above. In this group of measured events there were found:

6,700 inelastic scatterings and elastic scatterings with
a scattering angle of less than 13.2°,

2,114 p-p elastic scatterings,

584 π^+-p elastic scatterings, and

405 unknown elastic scatterings with a scattering angle
greater than 13.2°.

A δ ray of energy 1.66 Mev has a range of 1.7 cm in propane.
To scan for δ rays for length greater than 1.7 cm in true space, two
factors had to be considered. The first was that the demagnification
of a track on the film is a function of the depth of the track in the
chamber. Because all of the tracks scanned had already been measured,
a correction for the varying degree of demagnification was easy to cal-
culate. The second factor to be considered was that the track length
of the δ rays could be foreshortened due to the δ ray track dipping
either toward or away from the camera. To calculate the greatest amount
of foreshortening that was possible, the following calculation was made:

Consider the following illustration:
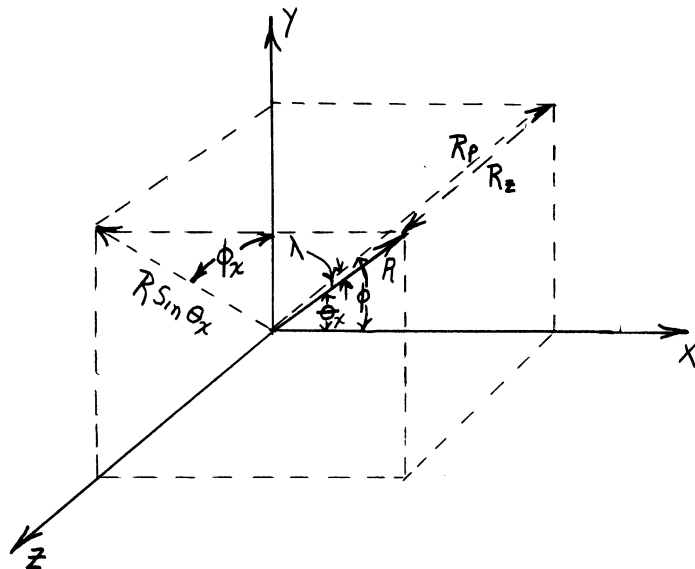
Let x be the incident beam direction,

y be the vertical direction,

z be the depth direction,

Θ_x be the polar angle about the x axis (the scattering angle),

ϕ_x be the azimuthal angle about the x axis,

λ be the dip angle,

ϕ be the azimuthal angle about the z axis, and

Rp be the projected range (that seen on the film).

(Note: Rx, R and R sin Θx lie in the same plane.)

Then

$$R_x = R \cos \Theta_x = R \cos\lambda \cos\phi$$

$$R_y = R \sin \Theta_x \cos \phi_x = R \cos \lambda \sin\phi$$

$$R_z = R \sin \Theta_x \sin \phi_x = R \sin \lambda$$

and $\quad$ Rp = R cos λ

but $\cos \lambda = (1 - \sin^2\lambda)^{1/2}$

$$= (1 - \frac{R_z^2}{R^2})^{1/2}$$

$$= (1 - \sin^2 \Theta_x \sin^2 \phi_x)^{1/2}$$

Therefore Rp = $R(1 - \sin^2 \Theta_x \sin^2 \phi_x)^{1/2}$

The projected track length of a δ ray that cannot be produced by a beam

proton will be at a minimum when the true space range of the δ ray is

1.7 cm and its azimuthal angle, ϕ_x is 90°. Because the stereo angle

of the camera was 15°, this means if both films are scanned for δ rays,

the worst possible case would occur when the normal to the plane defined

by the beam track and the δ ray track made an angle of 90° - 15°/2 = 82.5°

with respect to the line connecting the camera lens and the location of

the δ ray. Thus, ϕ_x = 82.5°. By using Equation (6) we can calculate

that a 1.66 Mev electron will make an angle of 38° with respect to the

pion beam track. Thus,

$$Rp = R(1 - \sin^2 38° \sin^2 82.5°)^{1/2}$$

$$= 0.796 \ R$$

$$= 1.35 \text{ cm, for } R = 1.7 \text{ cm.}$$

A projected track of 1.35 cm located at the greatest depth of the chamber

would have a length of 0.564 cm on the film due to demagnification.

On the basis of the above analysis the scanners were told to

scan for all δ rays with a projected range of greater than 0.40 cm.

They performed stereographic measurements to obtain the real space

ranges on all δ rays of range 0.40 cm $\leq$ R $\leq$ 1.7 cm x (demagnification

factor).

V. ANALYSIS OF ERRORS, BIASES AND CONTAMINATIONS

1. Scanning

A. Absolute Scanning Efficiency

Each picture was scanned by at least two different scanners in order to increase the total scanning efficiency for the experiment and to obtain the scanning efficiency of the individual scanners. Assuming that all events are equally difficult to find, the method used to obtain the scanning efficiency based upon the rescanning is given below:

Let N_1 = number of events scanner 1 finds,

N_2 = number of events scanner 2 finds,

N_{12} = number of events scanner 1 and 2 find in common,

N = true number of events in the pictures scanned,

e_1 = scanning efficiency of scanner 1, and

e_2 = scanning efficiency of scanner 2.

Then $N_1 = e_1 N$

$N_2 = e_2 N$

$N_{12} = e_1 e_2 N$

Therefore $e_1 = N_{12}/N_2$

$e_2 = N_{12}/N_1$

and the total scanning efficiency is given by:

Total Efficiency = $1 - (1 - e_1)(1 - e_2)$

By using this method the total scanning efficiency was greater than 99%.

B. Relative Scanning Efficiency

In the above analysis we have assumed that all events were equally difficult to find. This obviously is not true. The class of

events which consisted of small angle scatterings in which the plane

of the scattering was perpendicular to the plane of the windows was more

easily missed than the class of events in which the scattering angles

were large and the plane of the scatterings was parallel to the plane

of the windows. To test whether the scanning efficiency was uniformly

lower for the former mentioned geometry, all identified elastic scatter-

ings were divided into eight groups according to their scattering angle.

Then for each group of scatterings a histogram was made which correlated

the azimuthal angles of the scattering to number of scatterings for each

azimuthal increment. Two representative histograms are shown in Fig-

ure 16. An azimuthal angle of $\phi = 0°$ corresponds to the scattering

plane being perpendicular to the glass windows, and $\phi = 90°$ corresponds

to the scattering plane being parallel to the windows. The columns in

each histogram should be of equal height because of the manner in which

the azimuthal angle was computed, i.e., $0° \leq \phi \leq 90°$ rather than $0°$

$\leq \phi \leq 360°$. It can easily be seen that a differential azimuthal scan-

ning bias does exist, indicating there were classes of events in which

the scanning efficiency was uniformly lower than for other classes. On

the basis of these graphs, a differential scanning efficiency was then

computed. It was found that the relative scanning efficiency depended

upon the scattering angle as well as the azimuthal angle of scattering.

The differential scanning efficiency varied from 88% for pions scat-

tered in the backward direction to 98% for wide angle proton scatterings.

2. Measurement

Approximately 4% of the scatterings measured were remeasured

to determine the measuring efficiency of the girls. Two measurements of
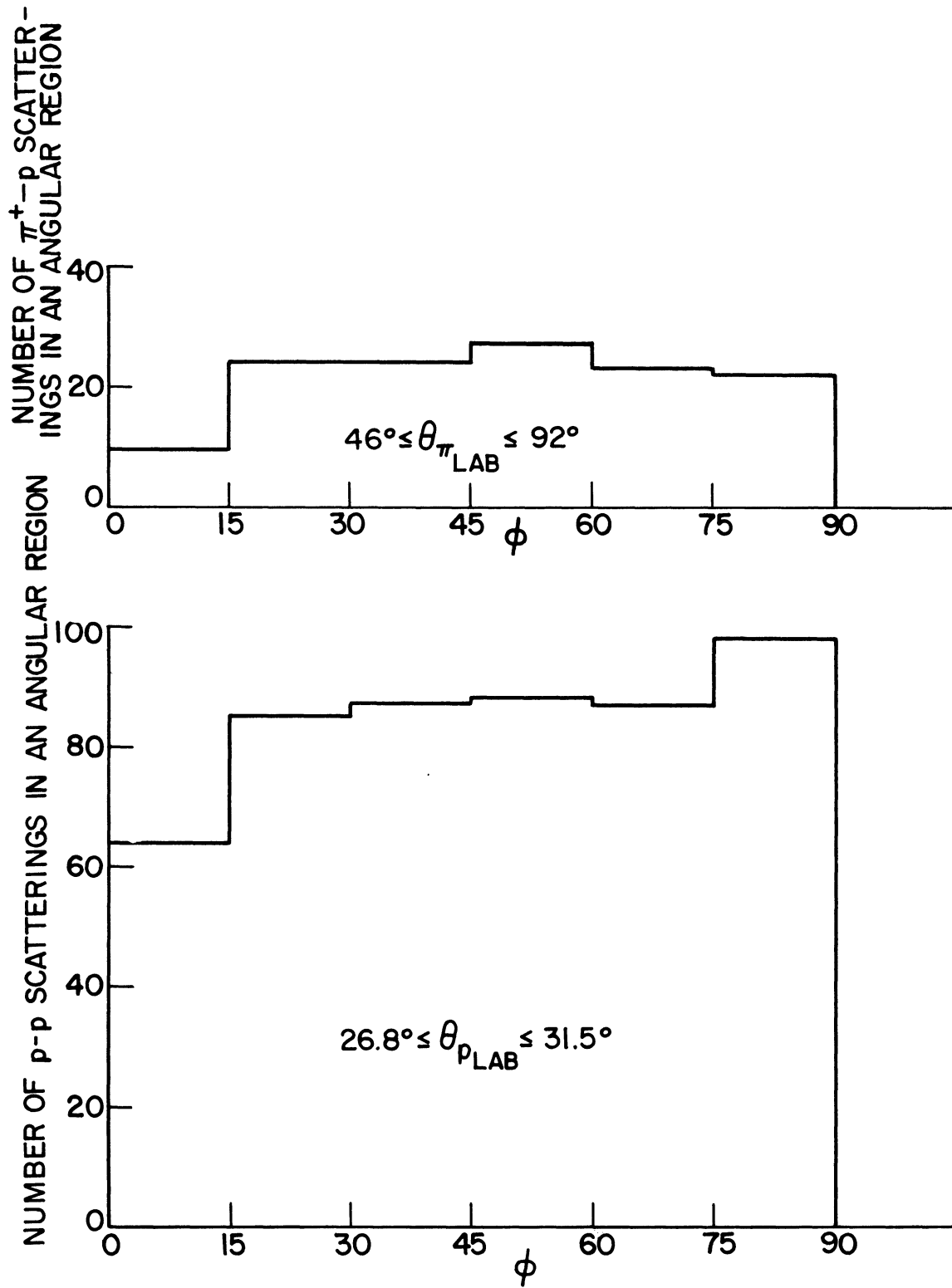
Figure 16. Representative Histograms Used for the Azimuthal Corrections

an event were considered to agree when the corresponding computed quantities (ϕ, θ_1, θ_2, etc.) of each measurement differed by no more than the sum of their errors. By this method the measuring efficiency was found to be $94 \pm 2\%$.

3. Carbon Contamination

Since approximately two-thirds of the total number of protons in the chamber are protons bound in carbon, the possibility that some of the accepted events might be grazing collisions in carbon, rather than collisions with free protons, must carefully be considered. To obtain an estimate of the number of such quasi-elastic events produced in carbon, 1,748 two-prong stars, which satisfied the coplanarity criteria but which were not identified as elastic scatterings, were studied. (See Figure 17.) Since in most cases it is impossible to tell pion tracks from proton tracks, the larger angle has been plotted against the smaller. The upper part of the π^+-p and p-p kinematic curve have been folded over about the line $\theta_1 = \theta_2$.

The Fermi momentum of a proton bound in carbon is of the order of 190 Mev/c.[31] If these protons contributed significantly to the coplanar two-prong star background and possibly, therefore, to the accepted elastic events, Figure 17 would be expected to show a diffuse grouping of such events around the angular correlation curves. The width of this grouping is expected to be of the order of $\pm 190/1230$ radians $= \pm 9°$. Since no such grouping is observed, it appears that these quasi-elastic events do not make a large contribution to the background, and therefore, the latter must be due mainly to "obviously inelastic" events.
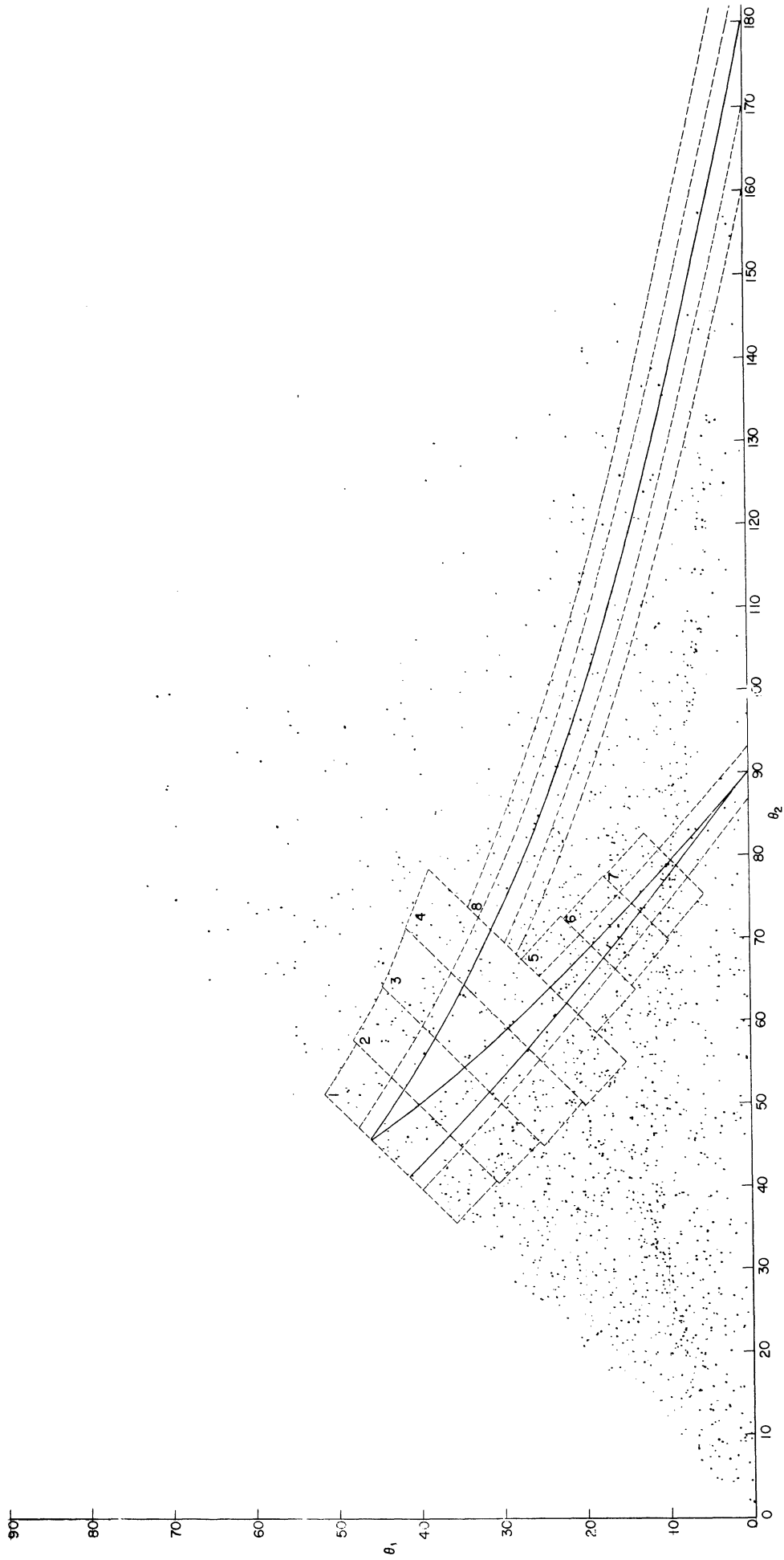
FIGURE 17
COPLANAR CARBON EVENTS

The usual method for obtaining carbon contamination in a propane bubble chamber experiment is to plot all coplanar carbon events on the angular kinematic curve for the reaction desired, and assume that the density of coplanar carbon events varies linearly in the region of the angular kinematic curve. Then if one has identified coplanar carbon events on or near the angular kinematic curve as "good" events, the density of coplanar carbon events will be lower in this region than it is in adjacent regions. By observing this fluctuation in density the carbon contamination can then be calculated. For example, consider the illustration below.
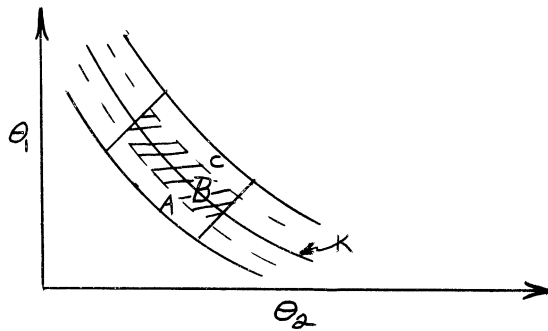
Let area B be an area that contains a large fraction of the "good" events. Let curve K be the angular kinematic curve for the desired reaction. Let area A and area C contain very few "good" events. Let area A = area C = area B/2. Let N_A = number of coplanar carbon events in area A, N_B = number of coplanar carbon events in area B, and N_C = number of coplanar carbon events in area C. Then the number of carbon events which were considered "good" events is $N_A + N_C - N_B$.

In this experiment the calculation of the carbon events was complicated because a differential carbon contamination was calculated for both the π^+-p and p-p scatterings. The assumption was made that the gradient of the density of coplanar carbon events was constant for

each angular differential region. (This constant, of course, varied

for each region.) Experimentally it was found $-3.1 \leq \dfrac{\frac{d\rho}{d\theta}}{\left[(d\theta_1)^2 + (d\theta_2)^2\right]^{1/2}} \leq 8.4$

where ρ is the density per unit area of coplanar carbon events.

The π^+-p elastic scattering kinematic curves were divided

into three regions, the p-p into six regions. Below is a table show-

ing the results of the carbon contamination calculations.

TABLE III

COMPUTED CONSTANTS USED TO DETERMINE THE CARBON CONTAMINATION

Region	N_A	N_B	N_C	$N_A + N_C - N_B$	$\dfrac{\frac{d\rho}{d\theta}}{\left[(d\theta_1)^2 + (d\theta_2)^2\right]^{1/2}}$	ρ_p	ρ_π
1	27	23	10	14	5.9	48	29
2	42	22	15	35	8.4	76	46
3	34	27	17	24	4.7	63	47
4	43	33	14	24	7.2	79	68,35
5	9	27	12	-6	-1.9		
6	14	32	10	-8			

ρ_p is the density of coplanar carbon events on the p-p curve as calcu-

lated from the density of coplanar carbon events in regions A and C.

ρ_π is the density of coplanar carbon events on the π^+-p curve as cal-

culated from the density of coplanar carbon events in regions A and C.

TABLE IV

CARBON CONTAMINATION OF p-p ELASTIC SCATTERINGS

Region	Angular Region	c	p	1 - c/p
1	$41.1 \geq \Theta p \geq 36.2$	11	440	$0.97 \pm 1\%$
2	$36.2 \geq \Theta p \geq 31.5$	13	359	$0.96 \pm 1\%$
3	$31.5 \geq \Theta p \geq 26.8$	9	446	$0.98 \pm 1\%$
4	$26.8 \geq \Theta p \geq 22.1$	11	445	$0.98 \pm 1\%$
5	$22.1 \geq \Theta p \geq 17.5$	-6	387	$1.01 \pm 1\%$
6	$17.5 \geq \Theta p \geq 13.2$	-6	303	$1.02 \pm 1\%$

TABLE V

CARBON CONTAMINATION OF π^+-p ELASTIC SCATTERINGS

Angular Region	c	π^+	1 - c/π^+
$13.2° \leq \Theta\pi \leq 19°$	-2	129	$1.01 \pm 3\%$
$19° \leq \Theta\pi \leq 71°$	48	403	$0.88 \pm 2\%$
$71° \leq \Theta\pi \leq 180°$	15	132	$0.89 \pm 3\%$

where c is the number of coplanar carbon events missing in the region of the p-p curve, p is the number of p-p scatterings in the angular region considered, and π^+ is the number of π^+-p scatterings in the angular region considered.

4. Beam Counting

The total number of tracks scanned was calculated by having the scanners count the beam tracks every twentieth picture. The total number of tracks scanned was about 234,000, and the mean number of tracks per picture was 25 with a standard deviation of 8.4. The standard error of the mean number of tracks per picture was calculated to be 0.39. Thus, the error in the total number of tracks scanned was 1.6%.

5. Beam Attenuation

Because the beam particles which entered the picture were counted to obtain the total length of beam scanned, a calculation had to be made to determine the attenuation of the beam in the chamber due to its interaction with the propane.

The total p-c, p-p, π^+-c and π^+-p cross sections have been measured at the momentum of this experiment.[3,18,33] They are:

$$\sigma_{t\,\pi^+-p} = 29 \pm 3 \text{ mb} \qquad \sigma_{t\,p-p} = 25 \pm 2 \text{ mb}$$

$$\sigma_{t\,\pi^--c} = 240 \text{ mb} \qquad \sigma_{t\,p-c} = 340 \pm 10 \text{ mb}$$

Knowing the above cross sections, the attenuation of the beam can easily be determined. It was found that the proton beam attenuation was 11% $\pm$ 1%, and the pion beam attenuation was 9%.

6. Summary

In Tables VI and VII are listed the differential errors, biases and contaminations that were discussed in this chapter for π^+-p and p-p scattering respectively.

TABLE VI

CORRECTIONS TO THE π^+-p CROSS SECTIONS

Interval	Azimuthal Correction	Muon Contamination	Beam Attenuation	Measuring Efficiency	Carbon Contamination	C
0.91 - 0.8	0.98 ± 0.5%	0.92 ± 3%	0.91 ± 1%	0.94 ± 2%	1.01 ± 3%	1.31 ± 5%
0.8 - 0.6	0.97 ± 0.5%	0.92 ± 3%	0.91 ± 1%	0.94 ± 2%	0.88 ± 2%	1.15 ± 4%
0.6 - 0.4	0.97 ± 0.5%	0.92 ± 3%	0.91 ± 1%	0.94 ± 2%	0.88 ± 2%	1.15 ± 4%
0.4 - 0.2	0.88 ± 4%	0.92 ± 3%	0.91 ± 1%	0.94 ± 2%	0.88 ± 2%	1.27 ± 6%
0.2 - 0.0	0.88 ± 4%	0.92 ± 3%	0.91 ± 1%	0.94 ± 2%	0.88 ± 2%	1.27 ± 6%
0.0 - -0.2	0.88 ± 4%	0.92 ± 3%	0.91 ± 1%	0.94 ± 2%	0.88 ± 2%	1.27 ± 6%
-0.2 - -0.4	0.88 ± 4%	0.92 ± 3%	0.91 ± 1%	0.94 ± 2%	0.89 ± 2%	1.28 ± 6%
-0.4 - -0.6	0.88 ± 4%	0.92 ± 3%	0.91 ± 1%	0.94 ± 2%	0.89 ± 3%	1.28 ± 6%
-0.6 - -0.8	0.89 ± 4%	0.92 ± 3%	0.91 ± 1%	0.94 ± 2%	0.89 ± 3%	1.27 ± 6%
-0.8 - -1.0	0.89 ± 4%	0.92 ± 3%	0.91 ± 1%	0.94 ± 2%	0.89 ± 3%	1.27 ± 6%

C is the total correction that must be added to the raw data cross section

$$\text{where } C = \frac{(\text{carbon contamination})}{(\text{measuring efficiency})(\text{azimuthal correction})(\text{beam attenuation})(\text{muon contamination})}$$

TABLE VII

CORRECTIONS TO THE p-p CROSS SECTIONS

Interval (Degrees)	Azimuthal Correction	Measuring Efficiency	Beam Attenuation	Carbon Contamination	C
30 - 40	0.99 ± 0.5%	0.94 ± 2%	0.89 ± 1%	1.02 ± 1%	1.23 ± 2.5%
40 - 50	0.97 ± 0.5%	0.94 ± 2%	0.89 ± 1%	1.01 ± 1%	1.25 ± 2.5%
50 - 60	0.985 ± 0.5%	0.94 ± 2%	0.89 ± 1%	0.98 ± 1%	1.18 ± 2.5%
60 - 70	0.96 ± 0.5%	0.94 ± 2%	0.89 ± 1%	0.98 ± 1%	1.22 ± 2.5%
70 - 80	0.98 ± 0.5%	0.94 ± 2%	0.89 ± 1%	0.96 ± 1%	1.17 ± 2.5%
80 - 90	0.98 ± 0.5%	0.94 ± 2%	0.89 ± 1%	0.97 ± 1%	1.18 ± 2.5%

$$C = \frac{(\text{carbon contamination})}{(\text{measuring efficiency})(\text{azimuthal correction})(\text{beam attenuation})}$$

VI. EXPERIMENTAL RESULTS

1. π^+-p Elastic Scattering

The differential cross section can be computed from the following relation:

$$\frac{d\sigma}{d\Omega} = \frac{C}{N x}\frac{dn}{d\Omega} = C\left(\frac{d\sigma}{d\Omega}\right)_{raw\ data} \tag{11}$$

where N is the number of protons per cc = 4.87×10^{22} cm^{-3},

x is the total pion length scanned = 1.726×10^6 cm,

dn is the number of pions observed to scatter into the solid angle $d\Omega$,

and C is the correction that must be made to the raw data as discussed in Chapter V.

In Table VIII the values of C, dn, $\frac{d\sigma}{d\Omega}$ (raw data) and $\frac{d\sigma}{d\Omega}$ are given for various increments of the cosine of the π^+ scattering angle in the center of mass system.

The differential cross section is plotted in Figure 18. On the vertical is plotted the differential cross section, and on the horizontal is plotted the cosine of the π^+ scattering angle in the center of mass system and also the corresponding scattering angle in the laboratory system.

It would be difficult to obtain the total elastic cross section from the above data because most of the cross section lies in the small angle scattering region. It is possible, however, to calculate the magnitude of the elastic differential cross section at 0° from the measurement of the total cross section. By the use of the well known optical
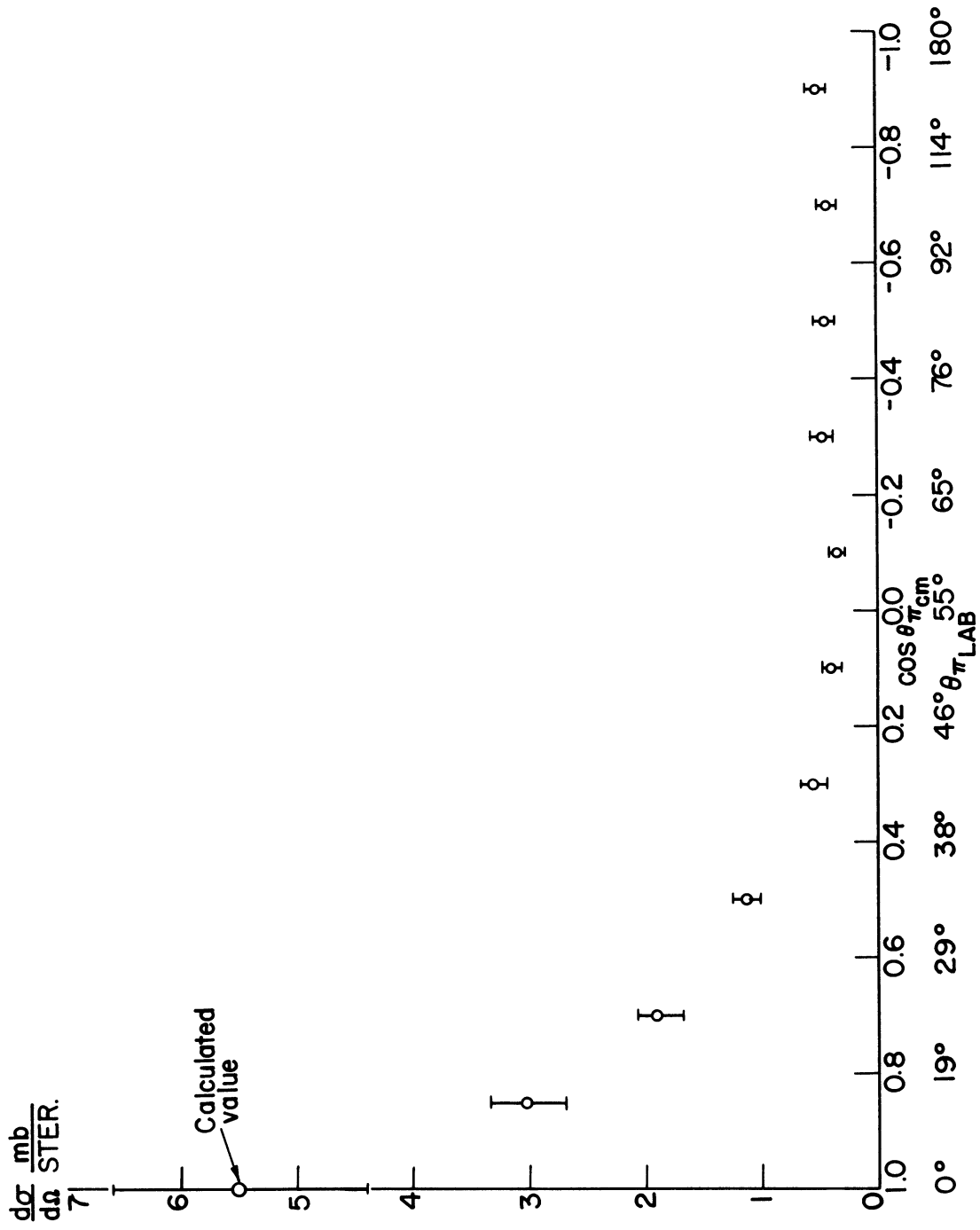
Figure 18. π^+-p Differential Cross Section at 1.1 Bev.

TABLE VIII

PARAMETERS FOR DETERMINING THE
π^{+}-p DIFFERENTIAL CROSS SECTION

$\Delta \cos \theta_{\pi}$ cm		dn	$\left(\dfrac{d\sigma}{d\Omega}\dfrac{mb}{ster.}\right)$ raw data	C	$\dfrac{d\sigma}{d\Omega}\left(\dfrac{mb}{ster.}\right)$
0.91-	0.8	129	2.30 $\pm$ 9%	1.31 $\pm$ 5%	3.01 $\pm$ 10%
0.8 -	0.6	172	1.63 $\pm$ 8%	1.15 $\pm$ 4%	1.87 $\pm$ 8%
0.6 -	0.4	103	0.97 $\pm$ 10%	1.15 $\pm$ 4%	1.12 $\pm$ 11%
0.4 -	0.2	44	0.42 $\pm$ 15%	1.27 $\pm$ 6%	0.53 $\pm$ 16%
0.2 -	0.0	33	0.31 $\pm$ 17%	1.27 $\pm$ 6%	0.39 $\pm$ 18%
0.0 -	-0.2	28	0.26 $\pm$ 19%	1.27 $\pm$ 6%	0.33 $\pm$ 20%
-0.2 -	-0.4	39	0.37 $\pm$ 16%	1.28 $\pm$ 6%	0.47 $\pm$ 17%
-0.4 -	-0.6	36	0.34 $\pm$ 17%	1.28 $\pm$ 6%	0.44 $\pm$ 18%
-0.6 -	-0.8	35	0.33 $\pm$ 17%	1.27 $\pm$ 6%	0.42 $\pm$ 18%
-0.8 -	-1.0	42	0.40 $\pm$ 15%	1.27 $\pm$ 6%	0.51 $\pm$ 16%

theorem one can calculate the imaginary part of the coherent forward
scattering amplitude. This amplitude is related to the total (elastic
and inelastic) scattering, σ_t by $\text{Im } f_c(0°) = k\sigma_t/4\pi$. The value of the
total cross section as given by Cool, Piccioni and Clark[3] is 28.8 x
10^{-27} cm^2 $\pm$ 10% and k, the propagation vector, is 3.25 x 10^{13} cm^{-1}.
Thus one finds $\left|\text{Im } f_c(0°)\right|^2 = (5.54 \pm 1.1)$ x 10^{-27} cm^2. The real part
of the coherent forward scattering amplitude was calculated by Stern-
heimer by means of the dispersion relations[35]. Sternheimer obtains
Re fc(0°) = 0. The coherent part of the elastic differential cross
section is therefore:

$$\frac{d\sigma_c(0°)}{d\Omega} = \left|\text{Re } f_c(0°)\right|^2 + \left|\text{Im } f_c(0°)\right|^2 = 5.5 \pm 1.1 \text{ mb/ster.}$$

The total forward elastic cross section is given by:

$$\frac{d\sigma(0°)}{d\Omega} = \frac{d\sigma_c(0°)}{d\Omega} + \frac{d\sigma(0°)}{d\Omega}\Big|_{spin\ flip}$$

If it is assumed that the only incoherent scattering process is nucleon spin flip scattering (see Chapter VII for a more complete discussion of this assumption), this process is characterized by a change in the Z component of the proton spin from $\pm$ 1/2 to $\mp$ 1/2. If the direction of the incoming pion is chosen as the axis of quantization, so that the incoming wave has no Z component of orbital angular momentum, conservation of angular momentum requires that the outgoing wave have a Z component, M_L, equal to $\pm$ 1. Since all spherical harmonics with $M_L = \pm 1$ are proportional to sin Θ, the spin flip scattering must vanish identically at $\Theta = 0°$. The elastic differential cross section at $0°$ is then

$$\frac{d\sigma_e(0°)}{d\Omega} = \frac{d\sigma_c(0°)}{d\Omega} = 5.5 \pm 1.1 \frac{mb}{ster.}$$

By using this calculated value the total cross section was found to be 12.3 $\pm$ 1.2 mb.

2. p-p Elastic Scattering

The differential cross section for p-p elastic scatterings was found by the use of Equation (11). The total proton track scanned was 3.000 x 10^6 cm, and the various values for c, dn and $\frac{d\sigma}{d\Omega}$ are given in Table 9.

In Figure 19 the differential p-p elastic cross section given above is plotted along with the values found by Nikitin, et al. at 560 Mev and Smith, et al. at 590 $\pm$ 15 Mev[17,18]. On the vertical is plotted the differential cross section, and on the horizontal is plotted
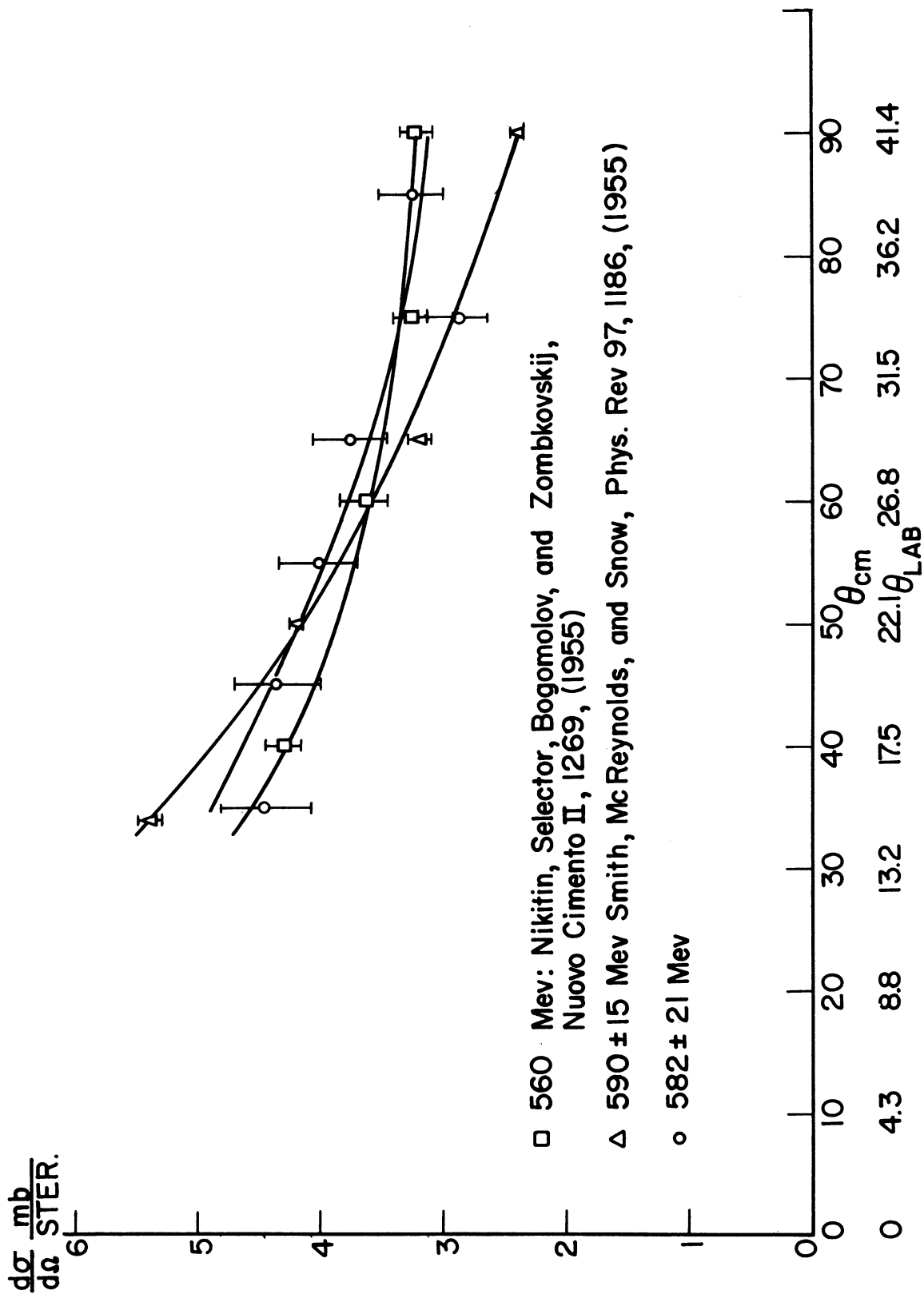
Figure 19. p-p Differential Cross Section at About 600 Mev.

TABLE 9

PARAMETERS FOR DETERMINING THE
p-p DIFFERENTIAL CROSS SECTION

Angular Interval in Center of Mass System	dn	c	$\frac{d\sigma}{d\Omega}\left(\frac{mb}{ster.}\right)$
30° - 40°	332 ± 5.5%	1.23 ± 2.5%	4.45 ± 0.36
40° - 50°	394 ± 5%	1.25 ± 2.5%	4.36 ± 0.35
50° - 60°	446 ± 5%	1.18 ± 2.5%	4.02 ± 0.32
60° - 70°	448 ± 5%	1.22 ± 2.5%	3.77 ± 0.30
70° ← 80°	380 ± 5%	1.17 ± 2.5%	2.88 ± 0.23
80° - 90°	442 ± 5%	1.18 ± 2.5%	3.27 ± 0.26

the scattering angle in the center of mass system. It can be seen that there is agreement between this bubble chamber experiment and the values found by counter experiments.

To obtain the total p-p elastic cross section the differential cross section was plotted as a function of the cos Θ_{cm}, where Θ_{cm} is the scattering angle in the center of mass system. (See Figure 20.) A straight line extrapolation was used to obtain the scattering cross section at small angles. The total cross section for elastic p-p scattering at 582 ± 21 Mev was found to be 24.2 ± 1.6 mb. Smith found a total cross section of 25 ± 2 mb at 590 ± 15 Mev [18].
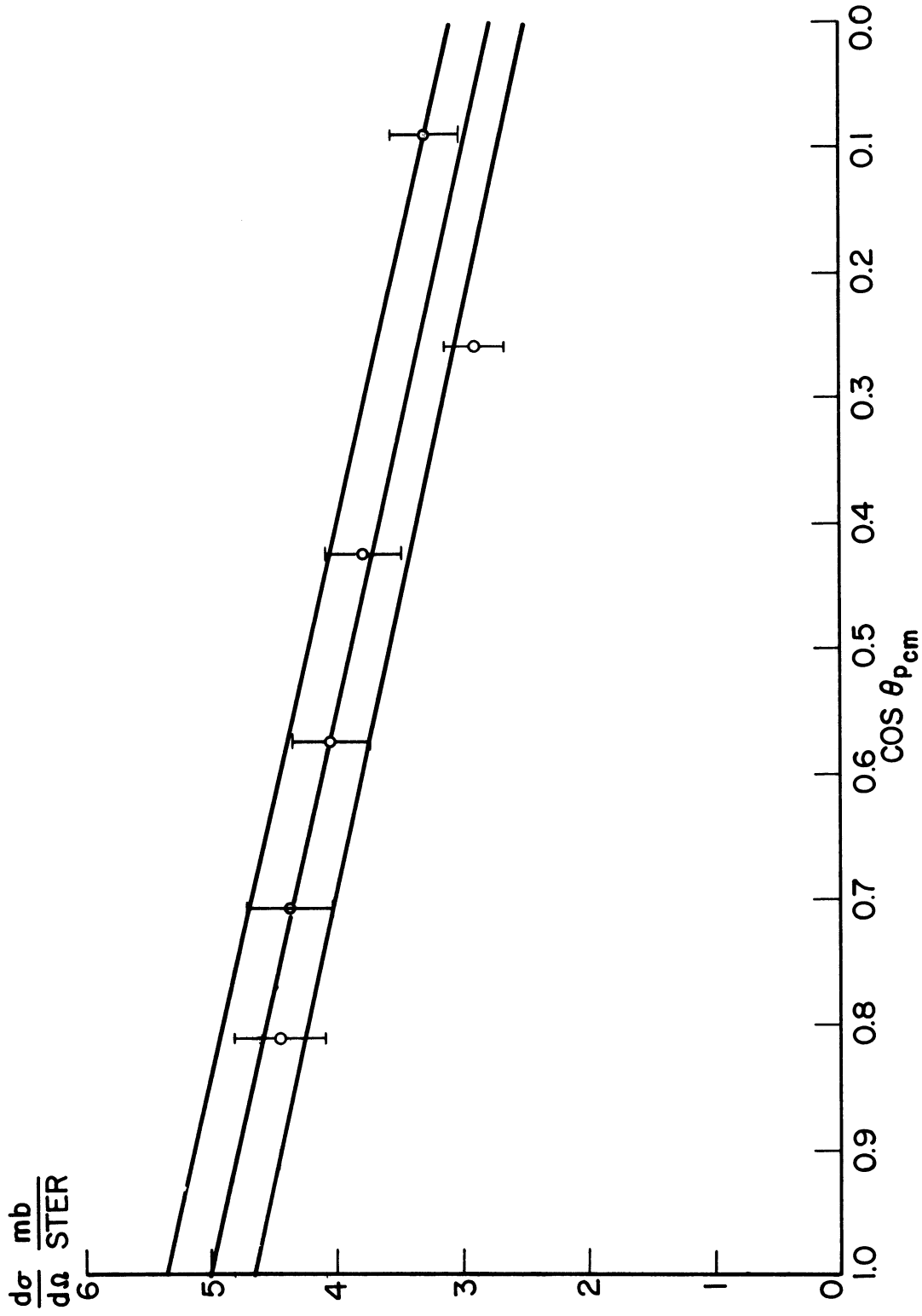
Figure 20. p-p Differential Cross Section at 582 $\pm$ Mev as a
Function of Cos $\theta_{p \, cm}$

VII. INTERPRETATION OF THE DATA

The π^+-p experimental data in Chapter VI will be interpreted in terms of the optical model[36,38]. A brief description of this model in terms of pion-proton scattering will be given below:

π^+-p interactions can be thought of in terms of a plane wave (the pion) incident upon an absorbing body (the proton). Part of the incident wave can be absorbed, and part of it can be scattered. The absorbed wave corresponds to inelastic or incoherent scattering, whereas the scattering wave corresponds to elastic, coherent, or diffraction scattering. At first, for simplicity, assume the absorbing body is a disk of radius R and thickness T. Let us also assume there is a boundary layer at the surface of the disk in which k_1 and K rise to their interior values in a distance larger than $1/k$, where k is the propagation vector of the pion wave outside of the proton, and its propagation vector inside is $k + k_1$ where

$$k_1 = k\left[\left(1 - \frac{V}{E}\right)^{1/2} - 1\right]$$

(12)

K is the absorption coefficient for proton matter. There will then be no scattering at the surfaces, and if we choose the amplitude of the incident wave to be unity, the wave transmitted through the disk will have an amplitude and relative phase $a = e^{\left(-\frac{K}{2} + ik_1\right)T}$.

The region of the shadow must contain a wave of lessened amplitude, a, whose intensity decrease gives the total incoherent absorption cross section, simply the total contribution to $1 - |a|^2$ integrated over the whole area of the disk. This is $\sigma_a = \pi R^2(1 - |a|^2)$.

To obtain the coherent or diffraction scattering, one has instead to
find the net amplitude which, added to the incident plane wave in the
shadow region, will yield the transmitted amplitude a. This is $(1 - a)$,
and it gives a total diffraction cross section of $\sigma = \sigma R^2 \left|1-a\right|^2$. The
scattering just mentioned is the well known Fraunhofer diffraction
scattering.

To find the angular distribution of the amplitude of the
scattered wave far behind the absorbing body, all contributions to the
amplitude reaching a given image point must be assumed from every source
point in a plane wave of amplitude $(1 - a)$ within the geometrical shadow.
This can be done by the following method:

Let the z axis be in the direction of propagation of the
incident wave; let O be in the shadow area of the wavefront; and let
the amplitude be sought at a distant point P, which has the polar co-
ordinates (r_0, θ, ϕ). (See the illustration below.)
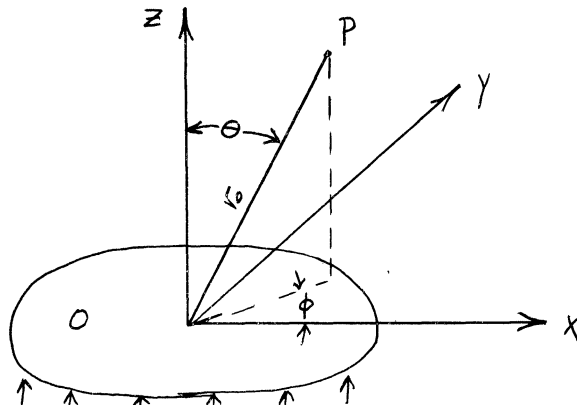
For $r_0 \gg$ the dimensions of the particle, the distance from
P to a point (x, y, o) of the shadow area is $r = r_0 - (x \cos \phi + y \sin \phi) \times \sin \theta$.

The spherical wave at P is then:

$$U_p = (1-a)\frac{k}{2\pi}\frac{e^{-ikr_0}}{r}\iint_{surface} e^{ik\left(x\cos\phi + y\sin\phi\right)\sin\theta}\,dx\,dy$$

where k is the propagation vector. Transforming to spherical coordin-
ates and integrating the angular part around a circle of radius ρ we
have

$$\iint\limits_{Surface} e^{ik\left(x\cos\phi + y\sin\phi\right)\sin\theta} dx\,dy = \int_{\rho=0}^{\rho=R} 2\pi J_0\left(k\rho\sin\theta\right)\rho\,d\rho \qquad (13)$$

$$= \frac{2\pi R}{k\sin\theta}\, J_1\left(k\,R\,\sin\theta\right)$$

Thus the amplitude can be written

$$f(\theta) = \left(1-a\right)R\,\frac{J_1\left(k\,R\,\sin\theta\right)}{\sin\theta}$$

and

$$\frac{d\sigma_d}{d\Omega} = \frac{\sigma_d}{\pi}\left|\frac{J_1\left(k\,R\,\sin\theta\right)}{\sin\theta}\right|^2 \qquad (14)$$

The corresponding calculations for a sphere are only slightly
more complicated. The portion of the wave which strikes the sphere at
a distance ρ from a line through the center of the sphere emerges after
traveling a distance 2s, with $s^2 = R^2 - \rho^2$. Its amplitude on emerging
is $a = e^{\left(-\frac{K}{2} + ik_1\right)2s}$, so that we have

$$\sigma_a = \int_0^{2\pi} d\phi \int_0^R \left(1 - e^{-2Ks}\right)\rho\,d\rho$$

$$= 2\pi \int_0^R \left(1 - e^{-2Ks}\right) s\,ds$$

$$= \pi R^2 \left\{1 - \frac{\left[1 - \left(1 + 2KR\right)e^{-2KR}\right]}{2K^2 R^2}\right\} \qquad (15)$$

The total diffraction cross section is now given by:

$$\sigma_d = 2\pi \int_0^R \left| 1 - e^{\left(-\kappa + 2ik_1\right)s} \right|^2 \rho \, d\rho$$

$$= \pi R^2 \left[1 + \left(\frac{1}{2\kappa^2 R^2}\right) \left\{ 1 - \left(1 + 2\kappa R\right) e^{-2\kappa R} \right\} \right.$$

$$- \frac{1}{\left(\frac{1}{4}\kappa^2 + k_1^2\right)^2 R^2} \left\{ \left(\frac{1}{4}\kappa^2 - k_1^2\right) + e^{-\kappa R}\left[2k_1 R\left(\frac{1}{4}\kappa^2 + k_1^2\right) + k_1 \kappa\right] \sin 2k_1 R \right.$$

$$\left. \left. - e^{-\kappa R}\left[\left(\frac{1}{4}\kappa^2 - k_1^2\right) + \kappa R\left(\frac{1}{4}\kappa^2 + k_1^2\right)\right] \cos 2k_1 R \right\} \right] \qquad (16)$$

In deriving (15) and (16), refraction at the surface of the sphere was neglected. Fernbach et al. mention that this is legitimate be-cause it only gives an error of order $\left(\frac{k_1}{k}\right)k_1 R$ (36).

The angular distribution in direct analogy to (13) is:

$$f(\theta) = k \int_{\rho=0}^{\rho=R} \left[1 - e^{\left(-\kappa + 2ik_1\right)s}\right] J_0\left(k\rho \sin\theta\right) \rho \, d\rho$$

For $K R \to \infty$, (14) is again obtained, but so far a convenient expression for the general case has not been found[36,38]. For purposes of calculation, Fernbach et al. have shown that the above integral can be converted to a sum by letting $\ell + 1/2 = k$ and using the relation $J_0\left[\left(\ell + \frac{1}{2}\right)\sin\theta\right] = P_\ell(\cos\theta)$, which is valid for large ℓ and small θ. They find

$$f(\theta) = \frac{1}{2k} \sum_{\ell=0}^{\ell + \frac{1}{2} < kR} \left(2\ell + 1\right)\left(1 - e^{\left(-\kappa + 2ik_1\right)s_\ell}\right) P_\ell(\cos\theta) \qquad (17)$$

where

$$S_\ell = \frac{\left[k^2 R^2 - \left(\ell + \frac{1}{2}\right)^2\right]^{1/2}}{k}$$

It should be noted that for dark grey spheres Equations (14) and (17) will give approximately the same values for the differential cross section.

To apply the optical model to the elastic scattering found in this experiment, one must be able to separate the incoherent elastic scattering from the coherent elastic scattering. Experimentally this was not possible, for in both cases the energy of the pion in the center of mass is the same before and after scattering. The incoherent elastic scattering was found by considering that after the pion and proton collide, they form a compound system, and at a later time a pion is emitted with the same energy in the center of mass system as the incoming pion. The phase of the emitted pion is random with respect to the phase of the incoming pion, and it should be emitted isotropically. For large angles, it is observed that the differential cross section is indeed isotropic. It was then assumed that this consists mainly of incoherent scattering, and this isotropic differential cross section, about 0.4 mb/ster., was subtracted from the differential cross section curve (Figure 18) to obtain the differential cross section curve for coherent scattering. (See Figure 22.) Integrating the coherent scattering curve, it was found that the diffraction cross section was 7.2 ± 0.8 mb. The incoherent elastic scattering along with the inelastic scattering should be considered as absorption scattering. The absorption cross section can be found by using the data of Cool, et al.[3] for the total cross section, $\sigma_t = 28.8 \pm 3$ mb. It is $\sigma_a = \sigma_t - \sigma_d = 28.8 - 7.2 = 21.6$ mb. It should be noted that the inelastic cross section, σ_i, will be

$$\sigma_i = \sigma_t - \sigma_e = 28.8 - 12.3 = 16.5 \text{ mb}.$$

Bethe and Wilson have evaluated $\sigma_d/\pi R^2$ and $\sigma_a/\pi R^2$ for various

values of $k_1\lambda$ [37], where k_1 and R have previously been defined, and λ

is the mean free path inside of the nucleon. Their curves are shown

in Figure 21. Now

$$\frac{\sigma_d/\pi R^2}{\sigma_a/\pi R^2} = \frac{\sigma_d}{\sigma_a} = \frac{7.2}{21.6} = 0.333$$

is the equation of a straight line. If it is assumed that there is no

potential scattering, so that $k_1\lambda = 0$, the intersection of the line

$\sigma_d/\sigma_a = 0.333$ with the curve for $k_1\lambda = 0$ will provide the values for

$\sigma_d/\pi R^2$ and $\sigma_a/\pi R^2$. Thus R, the radius of the proton, can be computed.

This procedure was carried out, and the radius of the proton

was found to be $R = 0.99^{+0.13}_{-0.11} \times 10^{-13}$cm. The opacity of the proton

$0 = \sigma_a/\pi R^2$ is then

$$0 = 0.70^{+0.06}_{-0.07} .$$

A check can be made on the value of R found by this method,

by putting R into Expression (17) and observing whether this expression

correctly predicts the angular distribution of the diffraction differ-

ential cross section.

To perform this calculation, K, the absorption coefficient

must be known. This can be calculated from Equation (15), for σ_a and

R are both known.

The angular distribution was calculated for $R = 0.99 \times 10^{-13}$cm,

and as can be seen from Figure 22, there is good agreement between the

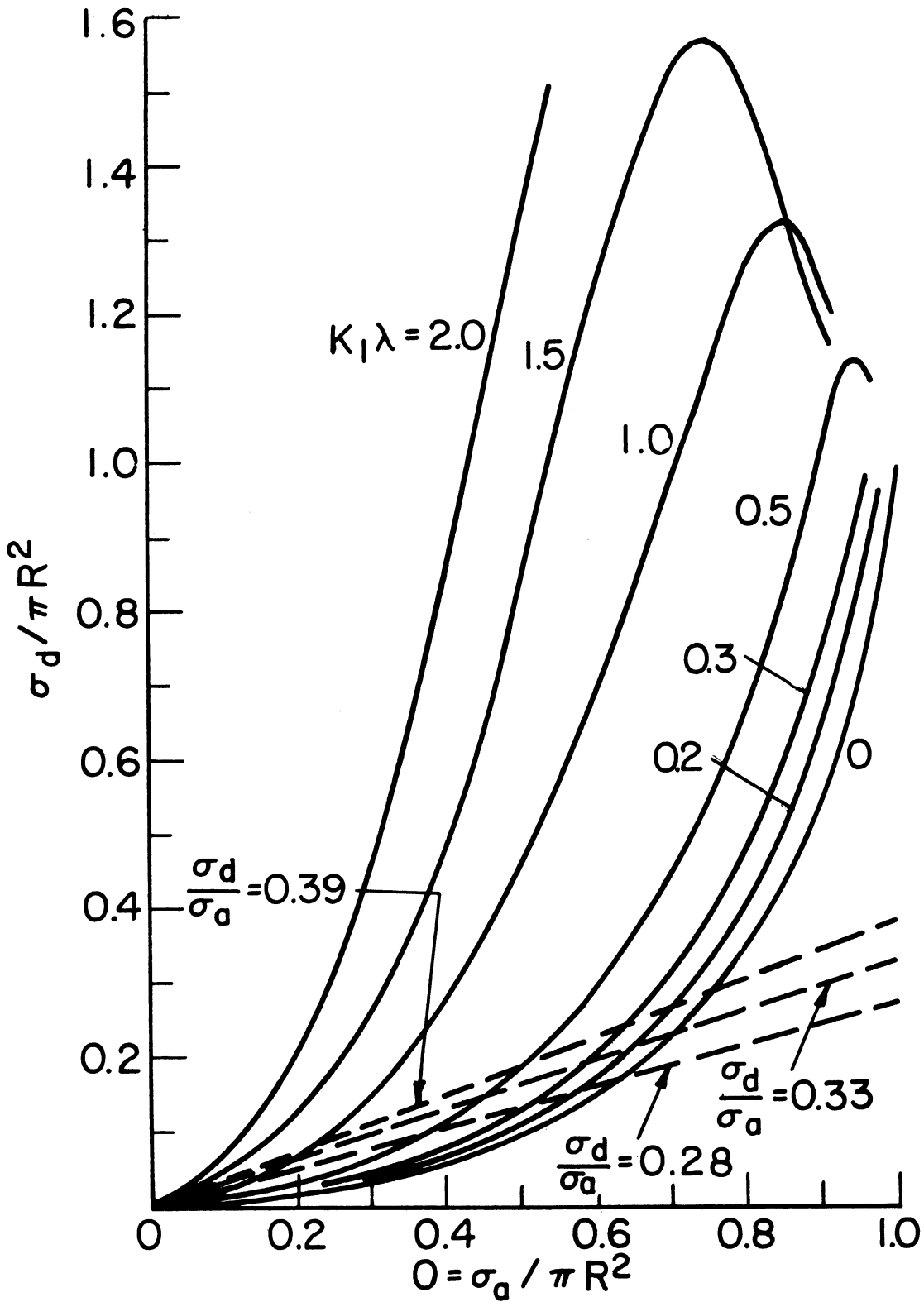experimental and optical model values for the diffraction cross section.

Figure 21. The Bethe, Wilson Curves with the Experimental
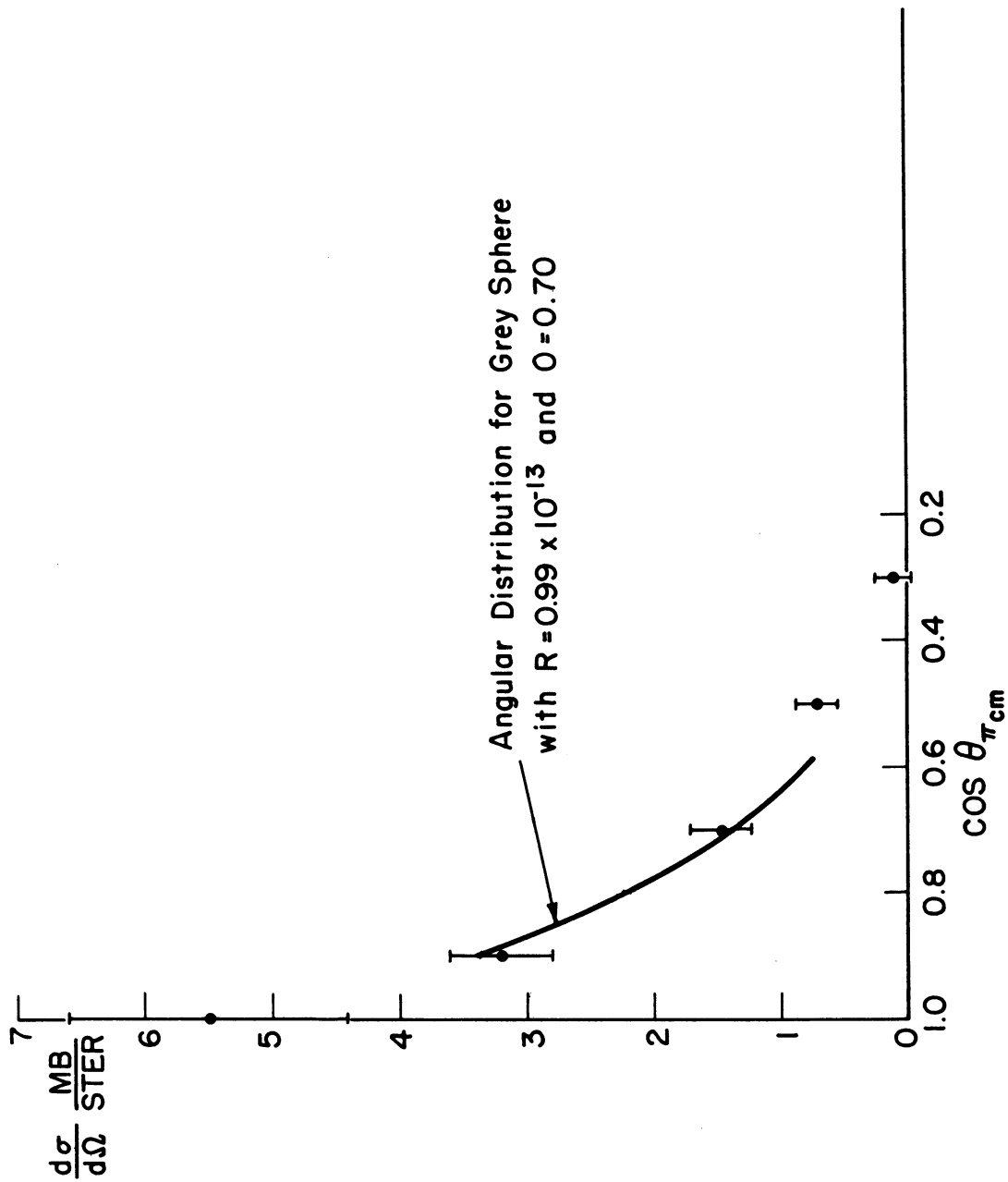Values for σ_d/σ_a = 0.333 ± 0.056.

Figure 22. Differential Cross Section for π^+ -p Diffraction
Scattering at 1.1 Bev.

The radius of the proton can also be found roughly by considering it a black body and fitting Expression (12) to the experimental angular distribution of the diffraction differential cross section. This was done, and an excellent fit was found for $R = 0.90^{+0.05}_{-0.04} \times 10^{-13}$ cm. (See Figure 23.) This method can only give an approximate result, for if the proton were a perfectly black body, the following expression would be true: $\sigma_d = \sigma_a = \pi R^2$. The experimental data shows this not to be true.

Below in Table X, a comparison will be found of the value of the radius of the proton and its opacity obtained by this experiment with the values obtained by the high energy π^--p scattering experiments.

TABLE X

EXPERIMENTAL VALUES FOR THE INTERACTION RADIUS
AND OPACITY OF THE PROTON

Type Interaction	Bombarding Energy	Interaction Radius in Fermis (10^{-13} cm)	Opacity	Reference
π^+-p	1.1 Bev	$0.99^{+0.13}_{-0.11}$	$0.70^{+0.06}_{-0.07}$	This experiment
π^--p	1.4	1.18 ± 0.10	0.61 ± 0.10	7
π^--p	1.85	$0.85^{+0.09}_{-0.03}$	$0.9^{+0.1}_{-0.2}$	12
π^--p	5	0.9 ± 0.15	0.6 ± 0.2	8

It is of some interest to compare the Stanford measurements of the electromagnetic size of the nucleon with the radius of the proton found in this experiment. For a number of assumed shapes for the distribution of the charge on the nucleon, Chambers and Hofstadter obtain
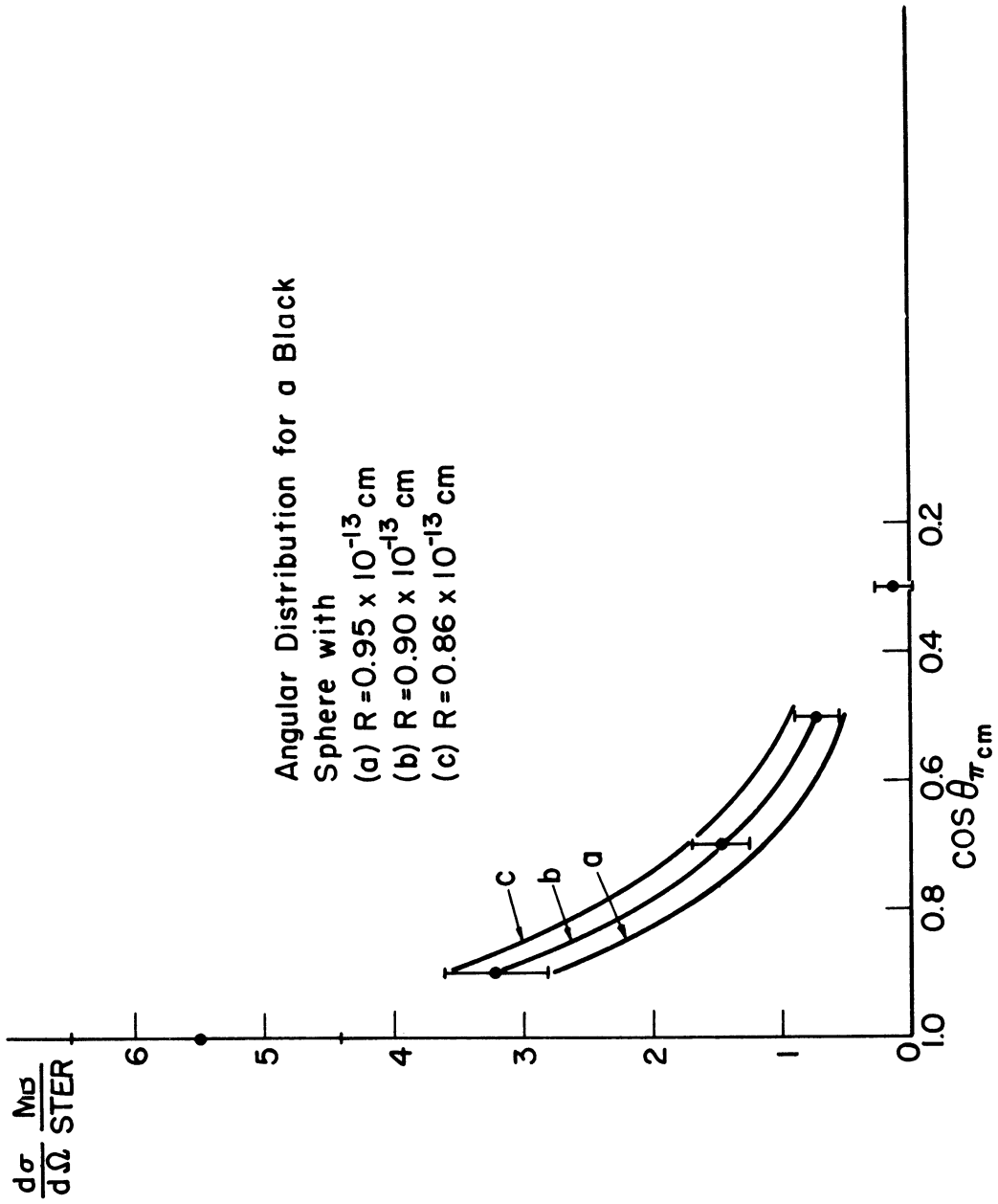
Figure 23. Differential Cross Section for π^+ -p Diffraction Scattering at 1.1 Bev.

$$(\langle r_e^2 \rangle_{Av})^{1/2} = 0.77 \pm 0.10 \text{ x } 10^{-13} \text{cm}.$$ [34] The r.m.s. value of the

proton found in this experiment is $0.77^{+0.10}_{-0.09}$ x 10^{-13}cm.

VIII. CONCLUSIONS

A total of 1.726×10^6 cm of pion track and 3.000×10^6 cm of proton track was scanned for elastic π^+-p interactions at 1.1 Bev and elastic p-p interactions at 582 Mev. This is the first high energy π^+-p elastic scattering result ever to be reported, whereas the p-p elastic scattering has already been measured in this energy region, and the p-p data will serve mainly to show that there was no large systematic bias in the previously reported counter experiments or in this experiment, since the biases are not likely to be identical.

On the basis of 661 identified π^+-p elastic scatterings the total elastic cross section and the angular distribution of the differential cross section were measured. The total elastic cross section was found to be 12.3 ± 1.2 mb. The angular distribution of the differential cross section was found to exhibit a peaking for small angle scattering and a rather isotropic distribution for large angle scattering. The optical model was then applied to the experimental data, and a proton interaction radius of $R = 0.99^{+0.13}_{-0.11} \times 10^{-13}$ cm was found to fit the data by two independent methods of calculation. The opacity of the proton was found to be $0 = 0.70^{+0.06}_{-0.07}$.

A total of 2,442 elastic p-p scatterings was observed. From this data a total cross section of 24.2 ± 1.6 mb was calculated. The angular distribution of the p-p elastic differential cross section was found to agree with that previously reported by counter experiments in this energy region.

IX. BIBLIOGRAPHY

1. Dyson, F.J., Phys. Rev., 99, 1037 (1955).

2. Takeda, G., Phys. Rev., 100, 440 (1955).

3. Cool, Piccioni and Clark, Phys. Rev., 103, 1082 (1956).

4. Goebel, C., Phys. Rev. Lett., 1, 337 (1958).

5. Bethe, H.A. and de Hoffmann, F., Mesons and Fields (Row, Peterson and Company, Evanston, 1955), Vol. II.

6. Walker, W.D. and Crussard, J., Phys. Rev, 98, 1416 (1955).

7. Eisberg, Fowler, Lea, Shephard, Shutt, Thorndike and Whittemore, Phys. Rev., 97, 797 (1955).

8. Maenchen, Fowler, Powell and Wright, Phys. Rev., 108, 850 (1957).

9. Walker, W.D., Phys. Rev., 108, 872 (1957).

10. Walker, Hushfar and Shephard, Phys. Rev., 104, 526 (1956).

11. Erwin, A. and Kopp, J., Phys. Rev., 109, 1364 (1958).

12. Whitten, R.C., and Block, M.M., Phys. Rev., 111, 1676 (1958).

13. Fermi, E., Progr. Theoret. Phys. (Japan) 5, 570 (1950); Phys. Rev., 92, 452 (1953); Phys. Rev., 93, 1434 (1954).

14. Fowler, Shutt, Thorndike, Whittemore, Cocconi, Hart, Block, Harth, Fowler, Garrison and Morris, Phys. Rev., 103, 1489 (1956).

15. Cork, Wenzel, Causey, Phys. Rev., 107, 859 (1957).

16. Morris, Rahm, Rau, Thorndike and Willis, Bull. Am. Phys. Soc., Ser. II, 3, 33 (1958).

17. Nikitin, Selector, Bogomolov and Zombkovskij, Nuovo Cimento II, 1269 (1955).

18. Smith, McReynolds and Snow, Phys. Rev., 97, 1186 (1955).

19. Duke, Loch, March, Gibson, McKeague, Hughes and Muirhead, Phil. Mag., 46, 877 (1955); Shapiro, Leavitt and Chen, Phys. Rev., 95, 663 (1954); Chen, Leavitt and Shapiro, Phys. Rev., 103, 212, (1956); Marshall, Marshall and Nedzel, Phys. Rev., 98, 1513 (1955); Ypsilantis, Wiegand, Tripp, Segre and Chamberlain, Phys. Rev., 98, 840 (1955); Sutton, Fields, Fox, Kane, Mott and Stallwood,

BIBLIOGRAPHY (CONT'D)

19. (Cont'd) Phys. Rev., 97, 783 (1955); Kane, Stallwood, Sutton, Fields and Fox, Phys. Rev., 95, 1694 (1954); Chamberlain, Segre, Tripp, Wiegand and Ypsilantis, Phys. Rev., 93, 1430 (1954); Dickson, J.M., and Salter, D.C., Nature, 173, 946 (1954); Marshall, Marshall and Nedzel, Phys. Rev., 93, 927 (1953); Chamberlain, Segre, and Wiegand, Phys. Rev., 83, 929 (1951); "Russian Experiments with 660-Mev Synchrocyclotron," Argonne National Laboratory, 1955. Translated by M. Hamermesh from Doklady Akad. Nauk U.S.S.R. 99, No. 6 (1954).

20. Rahm, D.C., Ph.D. Thesis, The University of Michigan, 1956 (unpublished).

21. Vander Velde, J.C., Ph.D. Thesis, The University of Michigan, 1957) (unpublished).

22. Yang, C.N., Proceedings of the Fifth Annual Rochester Conference on High Energy Physics, Interscience Press, Inc., New York (1955),p.37.

23. Abashian, Cool, Cronin and Piccioni (unpublished data).

24. Brookhaven National Lab. Report CCD-1.

25. Brookhaven National Lab. Report RMS-55.

26. Rossi, B., High Energy Physics, Prentice-Hall, New York (1952) p. 67.

27. Rahm, D., Bull. Am. Phys. Soc., Ser. II, 2, 11 (1957).

28. Chretien, Leitner, Samios, Schwartz and Steinberger, Phys. Rev., 108, 383 (1957).

29. Glaser, Rahm and Dodd, Phys. Rev., 102, 1653 (1956).

30. Bhabha, H.J., Proc. Roy. Soc. A., 164, 257 (1938).

31. Wattenberg, A., et al, Phys. Rev. (to be published).

32. Piccioni, O., 1958 Annual International Conference on High Energy Physics at Cern, (Cern, Scientific Information Service, Geneva, (1958)), p. 74.

33. Moskalev and Gavrilovskii, Doklady Akad. Nauk. U.S.S.R., 110, 972 (1956) (Translation: Soviet Physics "Doklady", 1, 607 (1956)).

34. Chambers, E., and Hofstadter, R., Phys. Rev., 103, 1454 (1956).

35. Sternheimer, R.S., Phys. Rev., 101, 384 (1956).

BIBLIOGRAPHY (CONT'D)

36. Fernbach, Serber and Taylor, Phys. Rev., 75, 1352 (1949).

37. Bethe, H.A., and Wilson, R.R., Phys. Rev., 83, 690 (1951).

38. Segre, E., Experimental Nuclear Physics, John Wiley and Sons, Inc.,
     New York (1953), p. 160.